

FlowPath: Learning Data-Driven Manifolds with Invertible Flows for Robust Irregularly-sampled Time Series Classification

YongKyung Oh¹, Dong-Young Lim^{2,3*}, Sungil Kim^{2,3*}

¹Medical & Imaging Informatics (MII) Group, University of California, Los Angeles (UCLA), CA, USA

²Department of Industrial Engineering, Ulsan National Institute of Science and Technology (UNIST), Republic of Korea

³Artificial Intelligence Graduate School, Ulsan National Institute of Science and Technology (UNIST), Republic of Korea
yongkyungoh@mednet.ucla.edu, {dlim, sungil.kim}@unist.ac.kr

Abstract

Modeling continuous-time dynamics from sparse and irregularly-sampled time series remains a fundamental challenge. Neural controlled differential equations provide a principled framework for such tasks, yet their performance is highly sensitive to the choice of control path constructed from discrete observations. Existing methods commonly employ fixed interpolation schemes, which impose simplistic geometric assumptions that often misrepresent the underlying data manifold, particularly under high missingness. We propose *FlowPath*, a novel approach that learns the geometry of the control path via an invertible neural flow. Rather than merely connecting observations, FlowPath constructs a continuous and data-adaptive manifold, guided by invertibility constraints that enforce information-preserving and well-behaved transformations. This inductive bias distinguishes FlowPath from prior unconstrained learnable path models. Empirical evaluations on 18 benchmark datasets and a real-world case study demonstrate that FlowPath consistently achieves statistically significant improvements in classification accuracy over baselines using fixed interpolants or non-invertible architectures. These results highlight the importance of modeling not only the dynamics along the path but also the geometry of the path itself, offering a robust and generalizable solution for learning from irregular time series.

Code — <https://github.com/yongkyung-oh/FlowPath>

Extended version — <https://arxiv.org/abs/2511.10841>

Introduction

Many real-world systems evolve continuously over time. In contrast, observations of these systems are typically sparse, irregular, and incomplete (Choi et al. 2016; Hossain, Ahad, and Inoue 2020; Oh, Lim, and Kim 2024). Such data are referred to as irregularly-sampled time series (ISTS), characterized by non-uniform sampling intervals and missing observations over time. While discrete-time models such as GRUs (Chung et al. 2014) have been adapted to handle irregularity using decay mechanisms (Che et al. 2018), they remain fundamentally discrete approximations. Neural Differential Equations (NDEs) address this limitation by modeling time as a continuous variable, with Neural Ordinary

Differential Equations (Neural ODEs) as a foundational case (Chen et al. 2018; Lu et al. 2018).

For ISTS, Neural Controlled Differential Equations (Neural CDEs) extend this idea by modeling system dynamics as driven by a continuous control path derived from the input (Kidger et al. 2020). Unlike Neural ODEs that evolve from an initial state (Rubanova, Chen, and Duvenaud 2019), Neural CDEs respond directly to the full input stream. However, the control path is typically constructed via fixed interpolation methods, which impose predefined geometric assumptions. This choice has been shown to affect performance substantially and remains a key limitation of the Neural CDE framework (Morrill et al. 2022).

In this paper, we propose *FlowPath*, a framework that models the control path using an invertible neural flow (Dinh, Sohl-Dickstein, and Bengio 2017; Papamakarios et al. 2021). This replaces the fixed interpolant with a learned, data-adaptive transformation that preserves invertibility. Such flows serve as universal approximators of diffeomorphisms (Teshima et al. 2020; Ishikawa et al. 2023), allowing the learned path to be smooth and information-preserving. We formalize the FlowPath architecture, analyze its theoretical properties, and evaluate it on 18 benchmark datasets and real-world datasets. Our results demonstrate that learning a structurally-constrained, data-driven manifold leads to statistically significant improvements in classification accuracy over baselines using either fixed interpolants or non-invertible learned paths.

Related Work

RNN-style Discretizations. Traditional Recurrent Neural Networks (RNNs) assume fixed step sizes (Goodfellow, Bengio, and Courville 2016), and adaptations such as GRU-D (Che et al. 2018) incorporate missingness indicators or time-lag decay to handle irregular sampling, but remain discrete-time approximations that can still struggle with large sampling gaps or nonuniform intervals. Thus, a conventional RNN or GRU-D processes data at sampled time points $\{t_k\}$. An RNN state $\mathbf{h}_k \in \mathbb{R}^{d_h}$ typically evolves via:

$$\mathbf{h}_{k+1} = \Psi(\mathbf{h}_k, \mathbf{x}_{k+1}, \Delta t_k),$$

where \mathbf{x}_{k+1} is the observation at time t_{k+1} and $\Delta t_k = t_{k+1} - t_k$. The function Ψ may incorporate gating or de-

*Corresponding Authors

cay terms to handle missingness and so remains a discrete approximation of an underlying continuous process.

NDE-based Models. To overcome the limitations of purely discrete-time methods, Chen et al. (2018) introduced Neural ODEs, casting hidden state evolution as a continuous function of time,

$$\frac{dz(t)}{dt} = f(t, z(t)), \quad z(0) = h(\mathbf{x}(0)).$$

The state $z(t) \in \mathbb{R}^{d_z}$ in a Neural ODE is obtained by integrating an initial value $z(0)$ from 0 to T . While this continuous viewpoint elegantly handles irregular time points, its strict reliance on the initial value problem makes it difficult to incorporate new observations arriving at later times without restarting or extending the integration (Rubanova, Chen, and Duvenaud 2019; Kidger 2022).

Neural CDEs (Kidger et al. 2020) overcome this limitation by representing the input time series as a control path $X(t) \in \mathbb{R}^{d_x}$, thereby enabling the hidden state to evolve continuously in response to incoming observations. The hidden state dynamics are governed by a Riemann–Stieltjes integral with respect to the control path:

$$z(t) = z(0) + \int_0^t f(\tau, z(\tau)) dX(\tau), \quad z(0) = h(X(0)).$$

Control path $X(t)$ is typically constructed from observed data using fixed interpolation methods such as linear or cubic splines (Morrill et al. 2021). This introduces a structural prior that may not align with the true dynamics. Empirical results show that interpolation choice is a sensitive hyperparameter with significant impact on performance, and no single method is optimal across tasks (Morrill et al. 2022).

Recent studies replace the fixed interpolant with a learned path from unconstrained networks, such as encoder-decoders (Jhin et al. 2022, 2023). Others apply attention mechanisms within the Neural CDE framework to reweight temporal contributions (Jhin et al. 2024). Further work focuses on improving the expressivity of the dynamics by signature transformation (Morrill et al. 2021). These approaches enhance flexibility but may introduce instability when the learned path lacks structural constraints.

Neural Flows. Bilos et al. (2021) propose modeling ODE solutions with an invertible transformation, circumventing numerical solvers by directly parameterizing a diffeomorphism in time. Such invertible mappings have been extensively studied in normalizing flows (Papamakarios et al. 2021), where tractable Jacobians enable density estimation or generative sampling. Formally, Neural Flow (Bilos et al. 2021) is designed to learn an invertible mapping $F(t, \mathbf{x}(0); \theta_F)$ that directly parameterizes the solution of an ODE or dynamical process. Given an implicit dynamical system governed by,

$$\frac{dz}{dt} = f(z(t)), \quad z(0) = \mathbf{x}(0),$$

Neural Flow posits a neural function F satisfying,

$$\frac{d}{dt} F(t, \mathbf{x}(0)) = f(F(t, \mathbf{x}(0))), \quad F(0, \mathbf{x}(0)) = \mathbf{x}(0).$$

Crucially, $F(\cdot)$ is designed to be a diffeomorphism in \mathbf{x} , ensuring that mapping local volumes is always invertible. This property allows Neural Flow to avoid the need for standard numerical ODE solvers and to guarantee the model’s Jacobian is tractable. While originally aimed at continuous normalizing flows for generative tasks, the concept of applying invertible flows to dynamic time series modeling has grown (Bilos et al. 2021; Oh, Lim, and Kim 2025).

Our approach builds on the observation that Neural CDEs and Neural Flows address complementary aspects of time series modeling. Instead of using a Neural Flow as an end-to-end model, we use it to construct a data-driven control path. This design combines the continuous-time formulation of NDEs with a learnable, invertible transformation that adapts to the observed data, avoiding the limitations of fixed interpolation schemes or unconstrained trajectories.

Methodology

We are given a dataset $\mathcal{D} = \{(\mathbf{X}_i, y_i)\}_{i=1}^N$, where each instance \mathbf{X}_i comprises a time-indexed sequence (t_i, \mathbf{x}_i) . Each $t_i \subset \mathbb{T}$ represents the set of sampling times, and $\mathbf{x}_i \in \mathbb{R}^{d_x}$ is the multivariate observation at those times. We aim to classify each instance with a label $y_i \in \{1, 2, \dots, K\}$. The sampling intervals $\Delta t_j = t_{j+1} - t_j$ are not necessarily uniform, and certain intervals may be missing data entirely. We aim to learn a predictive function $\mathcal{H} : (t_i, \mathbf{x}_i) \mapsto y_i$ that robustly classifies sequences under irregular sampling.

FlowPath Framework

Raw observation $\mathbf{x}(t)$ includes how missing values create discontinuities and distortions in the time series, disrupting its temporal structure. The proposed learnable flow $\Phi(t)$ generates a continuous path that preserves the underlying temporal dynamics. Unlike interpolation, which applies a fixed approach, the learnable flow adapts to surrounding patterns, leading to more informative representations for the downstream task.

Learning the Underlying Manifold. Let $F : [0, T] \times \mathbb{R}^{d_x} \rightarrow \mathbb{R}^{d_x}$ be a neural network parameterized by θ_F such that the mapping F is a diffeomorphism in its second argument (Bilos et al. 2021). We explicitly define the learnable control path $\Phi : [0, T] \rightarrow \mathbb{R}^{d_x}$ as:

$$\Phi(t) = F(t, \mathbf{x}; \theta_F), \quad (1)$$

where $\mathbf{x}(0) \in \mathbb{R}^{d_x}$ denotes the earliest available observation in the irregular time series. Unlike fixed spline-based interpolations, $\Phi(t)$ is parameterized by a neural network F with learnable parameters θ_F , allowing the control path to be learned directly from data in a flexible and adaptive manner.

Dynamics on the Learned Manifold. We define a hidden state $z(t) \in \mathbb{R}^{d_z}$ governed by the Riemann–Stieltjes integral as suggested by Kidger et al. (2020):

$$z(t) = z(0) + \int_0^t f(\tau, z(\tau); \theta_f) d\Phi(\tau). \quad (2)$$

Then, an equivalent ODE form of Eq. (2) defines:

$$\dot{z}(t) = f(t, z(t); \theta_f) \dot{\Phi}(t), \quad (3)$$

with $z(0) = h(x(0))$, and $h: \mathbb{R}^{d_x} \rightarrow \mathbb{R}^{d_z}$ an embedding layer. In Eq. (3), the dot notation $\dot{z}(t)$ and $\dot{\Phi}(t)$ denote the time derivatives, i.e., $\frac{dz(t)}{dt}$ and $\frac{d\Phi(t)}{dt}$, respectively. The smoothness assumptions on Φ guarantee Lipschitz continuity in time, while invertibility enforces distribution-preserving transformations (Papamakarios et al. 2021; Bilos et al. 2021). Since Φ is a diffeomorphism, the learned path $t \mapsto \Phi(t)$ admits well-defined inverses and Jacobians, which strengthen theoretical guarantees such as existence, uniqueness, and universal approximation for continuous-time processes. In practice, numerical solvers treat $\dot{\Phi}(t)$ as a known function (output of a neural net) and integrate $\dot{z}(t)$ forward in time, following the ODE form in Eq. (3).

Considerations for the Invertible Flow. We parameterize the control path using an invertible neural network based on normalizing flows, which provide a flexible framework for learning smooth, bijective transformations (Papamakarios et al. 2021). Recent theoretical results show that such architectures can approximate any diffeomorphism under suitable conditions (Teshima et al. 2020; Ishikawa et al. 2023). This ensures that the learned path $\Phi(t)$ remains invertible and smooth by design, reducing the risk of instability often seen in unconstrained path parameterizations.

Within the FlowPath framework, $\Phi(t) = F(t, x(0); \theta_F)$ acts as a trainable control path that modulates the evolution of the latent state $z(t)$. The function F is designed as an invertible neural network, drawing inspiration from normalizing flows (Papamakarios et al. 2021) and specifically neural flows that parameterize diffeomorphisms (Bilos et al. 2021). This design ensures that $\Phi(t)$ is a smooth transformation of its inputs, providing FlowPath with enhanced flexibility to model complex temporal dependencies.

Properties of FlowPath

The design of FlowPath results in a time-continuous model that (i) preserves information through an invertible flow, (ii) ensures well-posedness of the underlying dynamics, and (iii) promotes strong generalization capability. We present these three properties below, detailing full explanations in the supplementary material.

FlowPath uses an invertible flow Φ that reshapes the latent distribution without collapsing or tearing probability mass. The following theorem states that the instantaneous change in log-density is exactly driven by the divergence of the controlled dynamics, ensuring no unintended compression or expansion of probability mass.

Theorem 1 (Preservation of Probability Density). *Under the FlowPath framework in Eq. (2), let $\Phi(t)$ be a C^1 -diffeomorphism, and f be Lipschitz continuous in z . Then the probability density $p(z(t))$ of the latent state evolves according to*

$$\frac{d}{dt} \log p(z(t)) = -\operatorname{div}_z \left(f(t, z(t)) \dot{\Phi}(t) \right). \quad (4)$$

Consequently, Φ neither collapses nor arbitrarily expands probability mass, preserving the geometry of the latent distribution.

This property, while crucial for continuous normalizing flows in generative modeling (Papamakarios et al. 2021), also benefits our classification task by preserving class-separating structures in latent space, thereby improving robustness to irregular sampling and missing data.

Next, Theorem 2 establishes the standard existence and uniqueness guarantee for the FlowPath dynamics.

Theorem 2 (Existence and Uniqueness of Solutions). *Fix θ_f . Let $f(t, \cdot; \theta_f)$ in Eq. (2) be continuous in t and Lipschitz in z , and $\Phi(t)$ be continuously differentiable on $[0, T]$. Then for any initial condition $z(0) \in \mathbb{R}^{d_z}$, there exists a unique continuous solution*

$$z(t) = z(0) + \int_0^t f(s, z(s); \theta_f) d\Phi(s).$$

The universal approximation properties of Neural ODEs and Neural Flows have been extensively studied and established in prior work (Lin and Jegelka 2018; Li, Lin, and Shen 2022; Teshima et al. 2020; Ishikawa et al. 2023). Building upon these results, one can check that FlowPath is a universal approximator under appropriate regularity conditions. Under the assumption that Φ is a C^1 -diffeomorphism and f is Lipschitz, Neural ODEs are universal approximators for any smooth target trajectory u in the uniform norm. Thus, one can choose f such that within any desired precision ϵ'

$$\sup_{t \in [0, T]} \|f(t, z(t)) - \dot{\Phi}(t)^{-1} \dot{u}(t)\| < \epsilon'.$$

Substituting this into the FlowPath dynamics $\dot{z}(t) = f(t, z(t)) \dot{\Phi}(t)$ and integrating yields

$$\begin{aligned} \sup_{t \in [0, T]} \|z(t) - u(t)\| &\leq \int_0^T \|f(\tau, z(\tau)) \dot{\Phi}(\tau) - \dot{u}(\tau)\| d\tau \\ &\leq \int_0^T \left(\sup_{s \in [0, T]} \|\dot{\Phi}(s)\| \right) \epsilon' d\tau \\ &= \epsilon' \left(\sup_{s \in [0, T]} \|\dot{\Phi}(s)\| \right) T. \end{aligned}$$

Since $\sup_{t \in [0, T]} \|\dot{\Phi}(t)\|$ and T are finite, by choosing ϵ' appropriately, FlowPath can approximate any smooth trajectory to within arbitrary tolerance $\epsilon > 0$.

Let \mathcal{L} be an ℓ -Lipschitz loss in the model's final output. We parameterize FlowPath by $\theta = (\theta_f, \theta_F)$, where θ_f specifies the vector field f and θ_F defines the invertible flow Φ .

Theorem 3 (Generalization Bound). *Assume that the flow map $\Phi(\cdot; \theta_F): [0, T] \rightarrow \mathbb{R}^{d_x}$ is a diffeomorphism with $\sup_{t \in [0, T]} \|\dot{\Phi}(t)\| \leq M_\Phi$, and the vector field $f(\cdot, \cdot; \theta_f)$ is L_f -Lipschitz in the hidden state. Let \mathcal{F}_θ be the class of all such FlowPath predictors. Given n i.i.d. samples $\{(X_i, y_i)\}_{i=1}^n$ drawn from \mathcal{P} , define the population risk by*

$$\mathcal{R}_{\text{true}}(f) = \mathbb{E}_{(X, y) \sim \mathcal{P}} [\mathcal{L}(f(X), y)],$$

and the empirical risk by

$$\mathcal{R}_{\text{emp}}(f) = \frac{1}{n} \sum_{i=1}^n \mathcal{L}(f(X_i), y_i).$$

If $\hat{f} = \arg \min_{f \in \mathcal{F}_\Theta} \mathcal{R}_{\text{emp}}(f)$, then for any $\delta > 0$, with probability at least $1 - \delta$,

$$|\mathcal{R}_{\text{true}}(\hat{f}) - \mathcal{R}_{\text{emp}}(\hat{f})| \leq \alpha \frac{1}{\sqrt{n}} + \sqrt{\frac{\ln(1/\delta)}{2n}},$$

where α depends on ℓ , L_f , and M_Φ .

This result, derived via Rademacher complexity arguments (Bartlett, Foster, and Telgarsky 2017; Chen, Li, and Zhao 2020), indicates that, as the number of training samples n grows, the empirical loss of a FlowPath model closely approximates its true expected loss on unseen data.

Experiments

We design experiments to evaluate both the classification accuracy and robustness of our model under varying degrees of missing observations. Specifically, we consider 18 diverse time series classification datasets from UEA & UCR Data Repository, referenced in (Bagnall et al. 2018; H. A. Dau et al. 2019), utilizing the `sktime` Python library (Löning et al. 2019). We followed the experimental setup and dataset selection described by Oh, Lim, and Kim (2025). The original paper considered three categories: ‘Motion & Human Activity Recognition (HAR)’, ‘Electrocardiogram (ECG) & Electroencephalogram (EEG)’, and ‘Sensor’ domains, as summarized in the supplementary material.

In the experiments, three derivative datasets were created from each original dataset by artificially inducing missing data at rates of 30%, 50%, and 70%. Consequently, for each original dataset, there were four distinct settings, including the original data. The datasets were split into training, validation, and testing subsets, adhering to a 70/15/15 proportion. Lastly, the classification metrics were computed for each setting and averaged with five iterations.

Benchmark Methods

We utilized the conventional *RNN* (Medsker and Jain 1999), *LSTM* (S. Hochreiter and J. Schmidhuber 1997), and *GRU* (Chung et al. 2014), with mean imputation. Furthermore, we employed several modifications of the GRU, specifically *GRU- Δt* (Choi et al. 2016), *GRU-D* (Che et al. 2018), which have been tailored to efficiently handle ISTS. Additionally, we considered models that are based on the principles of Neural ODEs, such as *GRU-ODE* (Brouwer et al. 2019), *ODE-RNN* (Rubanova, Chen, and Duvenaud 2019) and *ODE-LSTM* (Lechner and Hasani 2020). Moreover, recent advancements of Neural CDEs were also included in the evaluation, such as *Neural CDE* (Kidger et al. 2020), *Neural RDE* (Morrill et al. 2021), *ANCDE* (Jhin et al. 2024), *EXIT* (Jhin et al. 2022), *LEAP* (Jhin et al. 2023), and *DualDynamics* (Oh, Lim, and Kim 2025). Lastly, we included naïve *Neural Flow* (Bilos et al. 2021) with different configurations: ResNet, GRU, and Coupling Flow.

Qualitative Evaluation of Key Properties

We used the ‘BasicMotions’ dataset for a qualitative analysis. The dataset comprises motion data collected from participants performing four distinct activities while wearing a

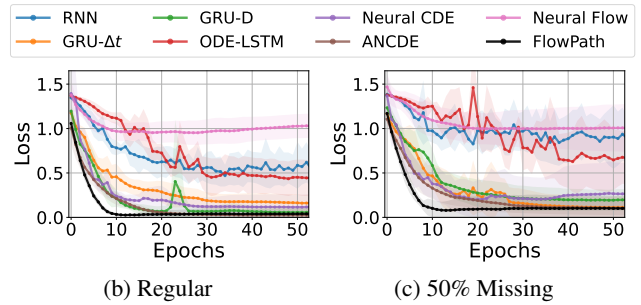


Figure 1: Test loss curves on ‘BasicMotions’ under regular and irregular scenarios using selected methods

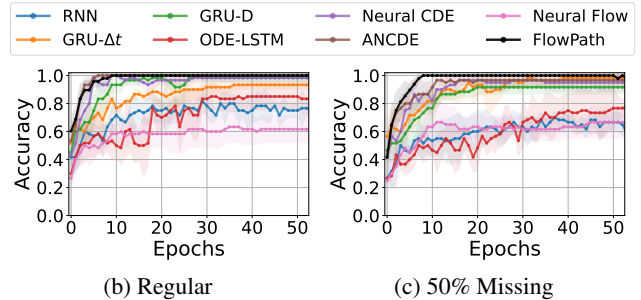
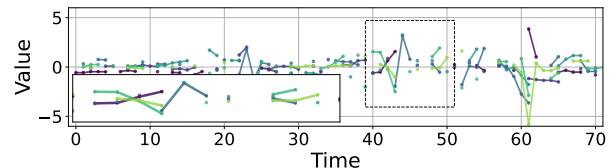
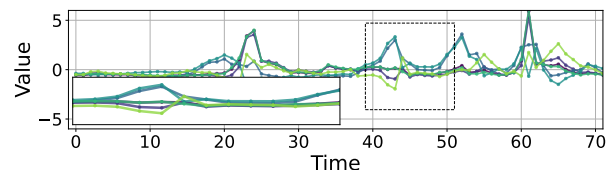


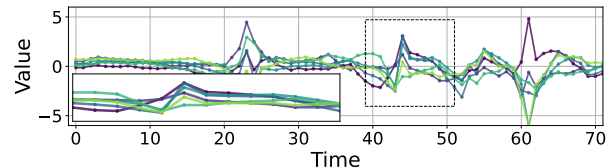
Figure 2: Test accuracy on ‘BasicMotions’ under regular and irregular scenarios using selected methods and FlowPath



(a) Irregularly-sampled time series (ISTS)



(b) MLP-based non-invertible path



(c) Flow-based invertible path

Figure 3: Qualitative comparison of path construction methods on a sample from the ‘BasicMotions’ dataset with 50% missingness. (a) Raw and sparse observations. (b) Path generated by a non-invertible MLP, exhibiting a biased curve toward the observed points. (c) Path produced by the proposed FlowPath, capturing a more structured and stable manifold. Each color denotes a separate data dimension.

smartwatch. Each activity was performed five times, with data sampled every 0.1 seconds over a 10-second period.

In Figures 1 and 2, FlowPath consistently achieves the lowest loss and highest accuracy, demonstrating faster and more stable convergence across both regular and missing data scenarios on the ‘BasicMotions’ dataset. This empirical observation of stable learning and robust performance aligns with FlowPath’s theoretical properties: the well-posedness of its dynamics (Theorem 2) contributes to stable training, while its generalization capability (Theorem 3) suggests that strong empirical performance can translate effectively to unseen test data.

Our goal is not to reconstruct the exact path but to learn a meaningful continuous representation $\Phi(t)$ for classification. Figure 3 shows a qualitative comparison of the manifolds learned from sparse data. Under highly irregular observations (a), a standard non-invertible multi-layer perceptron (MLP) (b) produces a disordered path that overfits sparse points without capturing the underlying structure. In contrast, FlowPath (c) learns a smoother and more coherent path. This stability arises from the invertibility constraint, which promotes information preservation and geometric consistency (Theorem 1). Additional visualizations are provided in the supplementary material.

Structural Comparison of Learned Manifolds

To assess the structure of the learned representations, we analyze trajectories and distributions. For clarity, three dimensions from the observation space are shown here. A full analysis is provided in the supplementary material. Furthermore, we include an extended discussion on NDEs’ robustness and manifold learning.

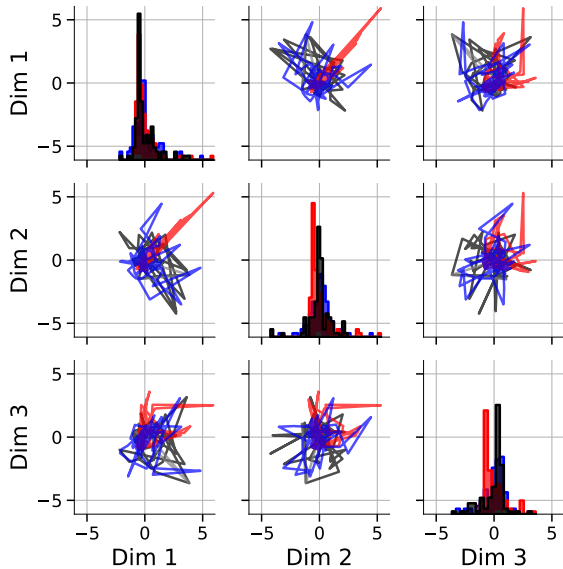


Figure 4: 2D projections of learned trajectories from sparse input. Off-diagonal plots show phase-space paths, and diagonal plots show marginal histograms. FlowPath (blue) better matches the ground truth (black) than the MLP (red).

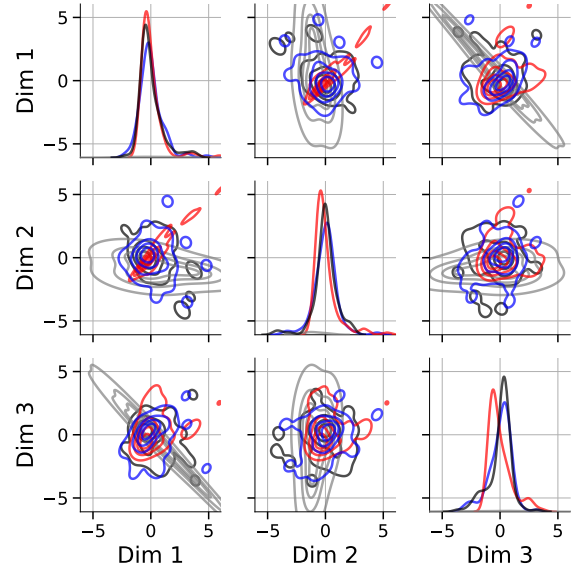


Figure 5: 1D and 2D Kernel Density Estimates (KDEs) for each method. FlowPath (blue) aligns more closely with the original distribution (black) than the MLP (red).

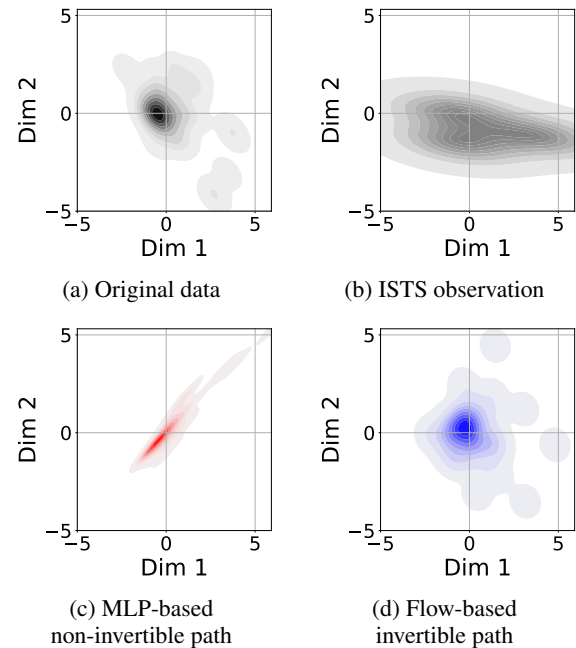


Figure 6: 2D KDEs of the learned manifolds between Dim 1 and Dim 2, using the sparse observation shown in panel (b)

Figure 4 highlights structural differences in the learned manifolds. Sparse observations (gray) lack temporal continuity due to missing data. The MLP path (red) shows instability and deviation from the original geometry (black), likely overfitting to observed points. FlowPath (blue), in contrast, maintains a smoother and more coherent trajectory, reflecting the benefits of the invertibility constraint.

Figure 5 shows KDEs of the learned manifolds. FlowPath achieves better alignment with the true distribution

Methods	Regular		30% Missing		50% Missing		70% Missing		Average	
	Accuracy	Rank	Accuracy	Rank	Accuracy	Rank	Accuracy	Rank	Accuracy	Rank
RNN	0.560 (0.072)	10.7	0.484 (0.075)	13.3	0.471 (0.082)	12.9	0.453 (0.068)	13.3	0.492 (0.074)	12.6
LSTM	0.588 (0.067)	10.0	0.552 (0.075)	9.4	0.516 (0.073)	10.5	0.505 (0.067)	10.6	0.540 (0.071)	10.1
GRU	0.674 (0.080)	6.9	0.639 (0.065)	8.0	0.611 (0.076)	8.2	0.606 (0.088)	8.1	0.633 (0.077)	7.8
GRU- Δt	0.629 (0.065)	9.1	0.636 (0.069)	7.6	0.651 (0.068)	6.7	0.649 (0.074)	7.5	0.641 (0.069)	7.7
GRU-D	0.593 (0.088)	10.0	0.579 (0.087)	9.8	0.580 (0.075)	9.7	0.599 (0.062)	9.4	0.588 (0.078)	9.7
GRU-ODE	0.663 (0.072)	7.2	0.661 (0.069)	6.8	0.664 (0.069)	6.5	0.659 (0.081)	6.3	0.662 (0.073)	6.7
ODE-RNN	0.652 (0.085)	6.8	0.632 (0.076)	7.3	0.626 (0.086)	7.2	0.653 (0.059)	5.8	0.641 (0.076)	6.8
ODE-LSTM	0.566 (0.074)	10.4	0.518 (0.069)	11.4	0.501 (0.068)	12.1	0.474 (0.068)	12.3	0.515 (0.070)	11.5
Neural CDE	0.681 (0.073)	7.1	0.672 (0.068)	7.3	0.661 (0.070)	7.0	0.652 (0.091)	7.0	0.667 (0.075)	7.1
Neural RDE	0.649 (0.082)	7.9	0.648 (0.071)	6.9	0.633 (0.078)	7.7	0.607 (0.079)	8.2	0.634 (0.078)	7.7
ANCDE	0.662 (0.083)	7.3	0.661 (0.083)	6.8	0.639 (0.080)	7.6	0.631 (0.073)	7.1	0.649 (0.080)	7.2
EXIT	0.595 (0.087)	9.4	0.580 (0.088)	9.8	0.578 (0.086)	9.5	0.564 (0.072)	10.0	0.579 (0.083)	9.7
LEAP	0.490 (0.062)	13.1	0.459 (0.070)	13.7	0.466 (0.074)	12.4	0.451 (0.074)	12.7	0.466 (0.070)	13.0
DualDynamics	<u>0.724 (0.090)</u>	<u>4.6</u>	<u>0.720 (0.088)</u>	<u>4.9</u>	<u>0.691 (0.091)</u>	<u>4.9</u>	<u>0.697 (0.098)</u>	<u>4.6</u>	<u>0.708 (0.092)</u>	<u>4.8</u>
Neural Flow	0.530 (0.069)	11.8	0.531 (0.072)	9.9	0.537 (0.073)	9.4	0.535 (0.082)	9.7	0.533 (0.074)	10.2
FlowPath	0.731 (0.083)	3.7	0.743 (0.091)	3.1	0.726 (0.084)	3.6	0.718 (0.090)	3.5	0.730 (0.087)	3.5

Table 1: Classification accuracy on 18 benchmark datasets under various scenarios. (Values in parentheses denote the mean standard deviation across different datasets and scenarios. **Best** and second-best results are highlighted, respectively.)

across both marginal and joint spaces. This ability to reconstruct distributional structure under sparsity contributes to its downstream classification performance. To illustrate this in detail, we zoom in on one representative case.

Figure 6 qualitatively analyzes the ability to recover the underlying manifold (a) from only the sparse observations in (b). The non-invertible MLP (c) learns a distorted distribution that is misaligned with the unknown original geometry. In contrast, FlowPath (d) yields a more coherent manifold that better aligns with the original distribution, suggesting that the structural constraint of invertibility is crucial for learning a faithful representation under sparsity.

Performance Comparison with 18 Datasets

In Table 1, we present a comparative analysis of average classification accuracy across various scenarios, including the regular scenario and irregular scenarios (with missing rates of 30%, 50%, and 70%), alongside an aggregate average across all settings. Notably, FlowPath maintains robustness under high rates of missing data, where other methods experience a significant performance drop. Additionally, FlowPath not only achieves the highest average accuracy but also consistently ranks among the top-performing models overall across the four missingness scenarios.

Settings	Regular	30% Missing	50% Missing	70% Missing	All Settings
Wins	8	11	11	10	40
Ties	2	1	2	1	6
Losses	8	6	5	7	26

Table 2: Pairwise comparison (wins / ties / losses) against DualDynamics across different missing rates.

As shown in Table 2, our method outperforms the strongest baseline, DualDynamics, under missing-value

conditions. Performance is similar in the regular setting, but our model gains more wins as the missing rate increases, showing greater robustness to incomplete observations. Complete baseline comparisons and pairwise statistical test results are provided in the supplementary material.

Table 3 presents an ablation study that investigates the sources of FlowPath’s performance improvements. The results indicate that while a simple learned path incorporated with an MLP yields modest gains over the fixed-path Neural CDE baseline, the structurally constrained FlowPath consistently achieves the highest performance across all levels of missingness. Furthermore, additional experiments reported in the supplementary material compare three invertible flow architectures, including ResNet, GRU, and Coupling Flow, demonstrating that FlowPath’s effectiveness is robust to the choice of flow architecture.

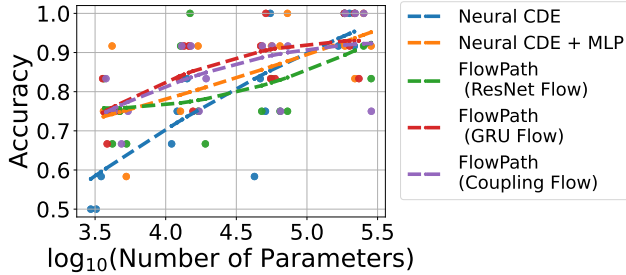
Settings	Regular	30% Missing	50% Missing	70% Missing	All Settings
Neural CDE	0.681 (0.073)	0.672 (0.068)	0.661 (0.070)	0.652 (0.091)	0.667 (0.075)
+ MLP	0.705 (0.077)	0.700 (0.084)	0.695 (0.091)	0.655 (0.084)	0.689 (0.084)
FlowPath	0.731 (0.083)	0.743 (0.091)	0.726 (0.084)	0.718 (0.090)	0.730 (0.087)

Table 3: Ablation study comparing the standard Neural CDE, a non-invertible MLP, and the proposed FlowPath.

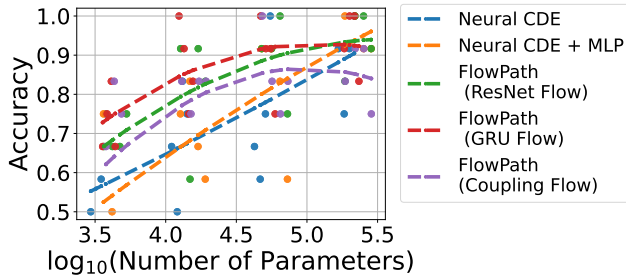
Performance-computation Analysis

We conduct an in-depth comparison across different hyperparameter settings, varying the flow architecture (ResNet, GRU, Coupling Flow), the number of layers n_l , and hidden sizes n_h . Figures 7 (a) and (b) compare classification accuracy to model complexity in the regular and 50% missing

settings, respectively. FlowPath variants consistently outperform the Neural CDE baseline at matched parameter counts, with performance gaps widening under higher missingness. MLP-based paths may perform adequately in certain cases; however, their performance significantly deteriorates under irregular scenarios. These results show that FlowPath’s invertible, learnable path improves performance with moderate computational cost, making it a practical choice.



(a) Performance on ‘Regular’ scenario



(b) Performance on ‘50% Missing’ scenario

Figure 7: Analysis of performance-computation trade-off. Figures show \log_{10} of the parameter count versus classification accuracy. Each colored dot corresponds to specific hyperparameters and the dashed line indicates the fitted trend.

Experiment: Real-world HAR Dataset

To evaluate robustness on a real-world task, we used the PAMAP2 dataset (A. Reiss and D. Stricker 2012), a challenging benchmark for sensor-based Human Activity Recognition (HAR). Each participant was equipped with three sensors positioned on the wrist, chest, and ankle, as well as a heart rate monitor. The dataset comprises 5333 segments spanning 8 daily living activities, captured using 17 distinct sensor modalities.

We followed the exact preprocessing protocol, data splits, and sensor dropout methodology proposed by Zhang et al. (2022). To simulate irregularity, we randomly removed 60% of data points from each segment, using the same random mask across all experiments. After that, we generated scenarios by randomly removing a subset of input sensors with dropout rates ranging from 10% to 50%. This approach increases the challenge of the problem, as the omitted sensors are randomly selected for each sample. For every test sample, a subset of sensors was designated as missing, and all observations from these sensors were replaced with zeros.

Benchmark Methods

We compare the proposed FlowPath with the following state-of-the-art baselines, including *Transformer* (Vaswani et al. 2017), *Trans-mean* (Transformer with mean imputation), *GRU-D* (Chen et al. 2018), *SeFT* (Horn et al. 2020), *mTAND* (Shukla and Marlin 2021), *Raindrop* (Zhang et al. 2022), and *Neural CDE* (Kidger et al. 2020).

For the original dataset without sensor dropout, we have included additional benchmarks such as *DGM²-O* (Wu et al. 2021), *IP-Net* (Shukla and Marlin 2019), *MTGNN* (Wu et al. 2020), *TITD* (Ji et al. 2025), and *CoFormer* (Y. Wei et al. 2023). For fair comparison, we used performance results as reported in the original literature.

Performance Comparison

As detailed in the supplementary material, optimal hyperparameters were selected via grid search. We employed the standard Neural CDE and compared various flow configurations for the proposed FlowPath. Regardless of the flow configuration, FlowPath consistently demonstrated superior classification performance compared to Neural CDE, as shown in Table 4. Based on hyperparameter tuning, the GRU Flow was selected for this dataset and scenarios.

Sensor Dropout	Neural CDE		FlowPath		
	Spline	MLP	ResNet	GRU	Coupling
0%	95.0 ± 0.4	93.9 ± 0.4	94.6 ± 0.5	95.6 ± 0.2	94.8 ± 0.2
10%	87.3 ± 1.3	86.4 ± 1.0	87.2 ± 0.3	88.3 ± 0.4	87.4 ± 0.3
20%	76.8 ± 0.6	75.1 ± 0.8	79.3 ± 1.0	79.1 ± 1.9	77.8 ± 0.6
30%	67.1 ± 1.9	68.2 ± 0.8	71.4 ± 0.7	70.0 ± 0.7	70.2 ± 1.0
40%	57.7 ± 1.6	58.8 ± 2.8	65.9 ± 1.9	59.6 ± 1.0	60.8 ± 1.1
50%	51.6 ± 1.0	50.7 ± 2.0	57.9 ± 0.2	54.1 ± 1.0	54.2 ± 3.1

Table 4: F1 score comparison on the PAMAP2 dataset between Neural CDE and the proposed FlowPath model.

Table 5 compares classification metrics for various methods under the irregularly-sampled PAMAP2 dataset with all sensors. FlowPath’s learnable invertible flow further boosts performance, indicating its superior handling of ISTS.

Methods	Accuracy	Precision	Recall	F1 Score
Transformer	83.5 ± 1.5	84.8 ± 1.5	86.0 ± 1.2	85.0 ± 1.3
Trans-mean	83.7 ± 2.3	84.9 ± 2.6	86.4 ± 2.1	85.1 ± 2.4
GRU-D	83.3 ± 1.6	84.6 ± 1.2	85.2 ± 1.6	84.8 ± 1.2
SeFT	67.1 ± 2.2	70.0 ± 2.4	68.2 ± 1.5	68.5 ± 1.8
mTAND	74.6 ± 4.3	74.3 ± 4.0	79.5 ± 2.8	76.8 ± 3.4
Raindrop	88.5 ± 1.5	89.9 ± 1.5	89.9 ± 0.6	89.8 ± 1.0
DGM ² -O	82.4 ± 2.3	85.2 ± 1.2	83.9 ± 2.3	84.3 ± 1.8
IP-Net	74.3 ± 3.8	75.6 ± 2.1	77.9 ± 2.2	76.6 ± 2.8
MTGNN	83.4 ± 1.9	85.2 ± 1.7	86.1 ± 1.9	85.9 ± 2.4
TITD	90.7 ± 0.5	90.2 ± 1.3	90.7 ± 0.9	90.5 ± 1.5
CoFormer	91.2 ± 0.6	92.4 ± 0.7	93.7 ± 0.7	92.8 ± 0.5
Neural CDE	<u>94.2 ± 0.5</u>	<u>95.2 ± 0.4</u>	<u>94.8 ± 0.5</u>	<u>95.0 ± 0.4</u>
FlowPath	94.8 ± 0.2	95.8 ± 0.4	95.5 ± 0.2	95.6 ± 0.2

Table 5: Classification performance on the PAMAP2 dataset with all sensors under original irregular sampling.

Furthermore, Table 6 summarizes the classification outcomes for the PAMAP2 dataset using a variety of benchmark methods. Across a comparison with all benchmark methods, our approach consistently delivers superior performance across all evaluated metrics.

	Methods	Accuracy	Precision	Recall	F1 Score
10% Missing	Transformer	60.9 ±12.8	58.4 ±18.4	59.1 ±16.2	56.9 ±18.9
	Trans-mean	62.4 ±3.5	59.6 ±7.2	63.7 ±8.1	62.7 ±6.4
	GRU-D	68.4 ±3.7	74.2 ±3.0	70.8 ±4.2	72.0 ±3.7
	SeFT	40.0 ±1.9	40.8 ±3.2	41.0 ±0.7	39.9 ±1.5
	mTAND	53.4 ±2.0	54.8 ±2.7	57.0 ±1.9	55.9 ±2.2
	Raindrop	76.7 ±1.8	79.9 ±1.7	77.9 ±2.3	78.6 ±1.8
	Neural CDE	<u>85.8 ±1.4</u>	<u>88.8 ±1.2</u>	<u>86.3 ±1.3</u>	<u>87.3 ±1.3</u>
	FlowPath	86.6 ±1.1	89.5 ±0.8	87.4 ±0.4	88.3 ±0.4
20% Missing	Transformer	62.3 ±11.5	65.9 ±12.7	61.4 ±13.9	61.8 ±15.6
	Trans-mean	56.8 ±4.1	59.4 ±3.4	53.2 ±3.9	55.3 ±3.5
	GRU-D	64.8 ±0.4	69.8 ±0.8	65.8 ±0.5	67.2 ±0.0
	SeFT	34.2 ±2.8	34.9 ±5.2	34.6 ±2.1	33.3 ±2.7
	mTAND	45.6 ±1.6	49.2 ±2.1	49.0 ±1.6	49.0 ±1.0
	Raindrop	71.3 ±2.5	75.8 ±2.2	72.5 ±2.0	73.4 ±2.1
	Neural CDE	<u>74.4 ±0.5</u>	<u>81.0 ±0.8</u>	<u>74.7 ±1.0</u>	<u>76.8 ±0.6</u>
	FlowPath	77.0 ±1.7	82.4 ±1.4	77.1 ±2.3	79.1 ±1.9
30% Missing	Transformer	52.0 ±11.9	55.2 ±15.3	50.1 ±13.3	48.4 ±18.2
	Trans-mean	65.1 ±1.9	63.8 ±1.2	67.9 ±1.8	64.9 ±1.7
	GRU-D	58.0 ±2.0	63.2 ±1.7	58.2 ±3.1	59.3 ±3.5
	SeFT	31.7 ±1.5	31.0 ±2.7	32.0 ±1.2	28.0 ±1.6
	mTAND	34.7 ±5.5	43.4 ±4.0	36.3 ±4.7	39.5 ±4.4
	Raindrop	60.3 ±3.5	68.1 ±3.1	60.3 ±3.6	61.9 ±3.9
	Neural CDE	<u>65.5 ±1.8</u>	<u>73.1 ±1.8</u>	64.9 ±2.3	<u>67.1 ±1.9</u>
	FlowPath	67.3 ±0.2	75.1 ±0.4	<u>67.7 ±0.7</u>	70.0 ±0.7
40% Missing	Transformer	43.8 ±14.0	44.6 ±23.0	40.5 ±15.9	40.2 ±20.1
	Trans-mean	48.7 ±2.7	55.8 ±2.6	54.2 ±3.0	55.1 ±2.9
	GRU-D	47.7 ±1.4	63.4 ±1.6	44.5 ±0.5	47.5 ±0.0
	SeFT	26.8 ±2.6	24.1 ±3.4	28.0 ±1.2	23.3 ±3.0
	mTAND	23.7 ±1.0	33.9 ±6.5	26.4 ±1.6	29.3 ±1.9
	Raindrop	<u>57.0 ±3.1</u>	65.4 ±2.7	<u>56.7 ±3.1</u>	<u>58.9 ±2.5</u>
	Neural CDE	55.8 ±0.5	67.7 ±1.5	54.5 ±2.3	57.7 ±1.6
	FlowPath	58.1 ±0.1	<u>67.0 ±0.9</u>	57.1 ±0.7	59.6 ±1.0
50% Missing	Transformer	43.2 ±2.5	52.0 ±2.5	36.9 ±3.1	41.9 ±3.2
	Trans-mean	46.4 ±1.4	59.1 ±3.2	43.1 ±2.2	46.5 ±3.1
	GRU-D	49.7 ±1.2	52.4 ±0.3	42.5 ±1.7	47.5 ±1.2
	SeFT	26.4 ±1.4	23.0 ±2.9	27.5 ±0.4	23.5 ±1.8
	mTAND	20.9 ±3.1	35.1 ±6.1	23.0 ±3.2	27.7 ±3.9
	Raindrop	47.2 ±4.4	59.4 ±3.9	44.8 ±5.3	47.6 ±5.2
	Neural CDE	<u>49.9 ±1.7</u>	<u>65.5 ±0.8</u>	<u>48.9 ±1.5</u>	<u>51.6 ±1.0</u>
	FlowPath	52.0 ±0.6	66.3 ±1.9	51.3 ±0.7	54.1 ±1.0

Table 6: Classification performance on the PAMAP2 dataset with sensor dropout rates ranging from 10% to 50%.

Experiment: Real-world Medical Dataset

We further evaluated model performance on a medical classification benchmark on the PhysioNet Sepsis dataset (Reyna et al. 2020), which includes 40,335 patients and 34 temporal variables. Following Kidger et al. (2020), we compared models with and without observation intensity

(OI), an index reflecting patient severity, and measured classification performance by AUROC.

Benchmark models and reported performance from Kidger et al. (2020), Oh, Lim, and Kim (2025), and Oh et al. (2025a). We also include variants of stable Neural SDEs (Oh, Lim, and Kim 2024), including Neural Langevin-type SDE (LSDE), Neural Linear Noise SDE (LNSDE), and Neural Geometric SDE (GSDE). For implementation details and benchmark methods, please consult the original studies.

Methods	Test AUROC	
	With OI	Without OI
GRU- Δt	0.878 ±0.006	0.840 ±0.007
GRU-D	0.871 ±0.022	0.850 ±0.013
GRU-ODE	0.852 ±0.010	0.771 ±0.024
ODE-RNN	0.874 ±0.016	0.833 ±0.020
Latent-ODE	0.787 ±0.011	0.495 ±0.002
ACE-NODE	0.804 ±0.010	0.514 ±0.003
Neural CDE	0.880 ±0.006	0.776 ±0.009
ANCDE	0.900 ±0.002	0.823 ±0.003
EXIT	0.913 ±0.002	0.836 ±0.003
DualDynamics	0.918 ±0.003	0.873 ±0.004
Neural SDE	0.799 ±0.007	0.796 ±0.006
Neural LSDE	0.909 ±0.004	0.879 ±0.008
Neural LNSDE	0.911 ±0.002	0.881 ±0.002
Neural GSDE	0.909 ±0.001	0.884 ±0.002
FlowPath		
– ResNet	0.919 ±0.005	0.869 ±0.006
– GRU	0.918 ±0.005	0.870 ±0.005
– Coupling	0.916 ±0.006	0.866 ±0.002

Table 7: AUROC Comparison on PhysioNet Sepsis

As shown in Table 7, FlowPath variants achieve the highest or near-highest AUROC among all baselines. These results suggest that learning continuous flow variations offers a reliable inductive bias for modeling complex temporal dynamics in time series analysis.

Conclusion

We present *FlowPath*, a framework for modeling ISTS by learning the control path of a Neural CDE through an invertible neural flow. This approach replaces fixed interpolation with a data-adaptive, structure-preserving transformation that more accurately captures the underlying temporal geometry. Experimental results on 18 benchmark datasets and a real-world case study demonstrate improved classification accuracy and robustness, particularly under conditions of high missingness. These findings highlight the importance of modeling the geometry of the control path, not just the dynamics along it, to build reliable continuous-time models for real-world applications.

While FlowPath improves robustness by learning a well-structured control path, its use of invertible flows introduces additional parameters. Exploring more efficient architectures could reduce this overhead. Furthermore, our evaluation also focuses on classification, and the performance of FlowPath on tasks such as forecasting and generative modeling remains an important area for future investigation.

Acknowledgments

We thank the teams and individuals for their efforts in the real-world dataset preparation and curation for our research, especially the UEA & UCR repository for the numerous datasets that we extensively analyzed.

This research was supported by Basic Science Research Program through the National Research Foundation of Korea (NRF) funded by the Ministry of Education (RS-2024-00407852); the Institute of Information & Communications Technology Planning & Evaluation(IITP) grant funded by the Korea government(MSIT)(No.RS-2020-II201336, Artificial Intelligence graduate school support(UNIST)); the Institute of Information & Communications Technology Planning & Evaluation(IITP) grant funded by the Korea government(MSIT) (No. RS-2025-25442824, AI STAR Fellowship); the National Research Foundation of Korea(NRF) grant funded by the Korea government(MSIT) (No.RS-2023-00218913, RS-2025-00563597, No. RS-2025-02216640)

References

- A. Reiss; and D. Stricker. 2012. Introducing a New Benchmarked Dataset for Activity Monitoring. In *2012 16th International Symposium on Wearable Computers*, 108–109.
- Bagnall, A.; Dau, H. A.; Lines, J.; Flynn, M.; Large, J.; Bostrom, A.; Southam, P.; and Keogh, E. 2018. The UEA multivariate time series classification archive, 2018.
- Bartlett, P. L.; Foster, D. J.; and Telgarsky, M. 2017. Spectrally-normalized margin bounds for neural networks. In *Advances in Neural Information Processing Systems 30: Annual Conference on Neural Information Processing Systems 2017, December 4-9, 2017, Long Beach, CA, USA*, 6240–6249.
- Behrmann, J.; Grathwohl, W.; Chen, R. T. Q.; Duvenaud, D.; and Jacobsen, J.-H. 2019. Invertible Residual Networks. In Chaudhuri, K.; and Salakhutdinov, R., eds., *Proceedings of the 36th International Conference on Machine Learning*, volume 97, 573–582. Proceedings of Machine Learning Research: PMLR.
- Benavoli, A.; Corani, G.; and Mangili, F. 2016. Should We Really Use Post-Hoc Tests Based on Mean-Ranks? *Journal of Machine Learning Research*, 17(5): 1–10.
- Bilos, M.; Sommer, J.; Rangapuram, S. S.; Januschowski, T.; and Günnemann, S. 2021. Neural Flows: Efficient Alternative to Neural ODEs. In *Advances in Neural Information Processing Systems 34: Annual Conference on Neural Information Processing Systems 2021, NeurIPS 2021, December 6-14, 2021, virtual.*, 21325–21337.
- Brouwer, E. D.; Simm, J.; Arany, A.; and Moreau, Y. 2019. GRU-ODE-Bayes: Continuous Modeling of Sporadically-Observed Time Series. In *Advances in Neural Information Processing Systems 32: Annual Conference on Neural Information Processing Systems 2019, NeurIPS 2019, December 8-14, 2019, Vancouver, BC, Canada.*, 7377–7388.
- Che, Z.; Purushotham, S.; Cho, K.; Sontag, D.; and Liu, Y. 2018. Recurrent Neural Networks for Multivariate Time Series with Missing Values. *Scientific Reports*, 8(1): 6085.
- Chen, M.; Li, X.; and Zhao, T. 2020. On Generalization Bounds of a Family of Recurrent Neural Networks. In *The 23rd International Conference on Artificial Intelligence and Statistics, AISTATS 2020, 26-28 August 2020, Online [Palermo, Sicily, Italy]*, 1233–1243.
- Chen, R. T. Q.; and Lipman, Y. 2024. Flow Matching on General Geometries. In *The Twelfth International Conference on Learning Representations, ICLR 2024, Vienna, Austria, May 7-11, 2024*.
- Chen, T. Q.; Rubanova, Y.; Bettencourt, J.; and Duvenaud, D. 2018. Neural Ordinary Differential Equations. In *Advances in Neural Information Processing Systems 31: Annual Conference on Neural Information Processing Systems 2018, NeurIPS 2018, December 3-8, 2018, Montréal, Canada.*, 6572–6583.
- Choi, E.; Bahadori, M. T.; Schuetz, A.; Stewart, W. F.; and Sun, J. 2016. Doctor AI: Predicting Clinical Events via Recurrent Neural Networks. In Doshi-Velez, F.; Fackler, J.; Kale, D.; Wallace, B.; and Wiens, J., eds., *Proceedings of the 1st Machine Learning for Healthcare Conference*, volume 56 of *Proceedings of Machine Learning Research*, 301–318. Northeastern University, Boston, MA, USA: PMLR.
- Chung, J.; Gulcehre, C.; Cho, K.; and Bengio, Y. 2014. Empirical Evaluation of Gated Recurrent Neural Networks on Sequence Modeling.
- Demšar, J. 2006. Statistical Comparisons of Classifiers over Multiple Data Sets. *Journal of Machine Learning Research*, 7(1): 1–30.
- Dinh, L.; Krueger, D.; and Bengio, Y. 2015. NICE: Non-linear Independent Components Estimation. In *3rd International Conference on Learning Representations, ICLR 2015, San Diego, CA, USA, May 7-9, 2015, Workshop Track Proceedings*.
- Dinh, L.; Sohl-Dickstein, J.; and Bengio, S. 2017. Density estimation using Real NVP. In *5th International Conference on Learning Representations, ICLR 2017, Toulon, France, April 24-26, 2017, Conference Track Proceedings*.
- Giacalone, M.; Agata, Z.; Cozzucoli, P. C.; and Alibrandi, A. 2018. Bonferroni-Holm and permutation tests to compare health data: methodological and applicative issues. *BMC Medical Research Methodology*, 18(1): 81.
- Goodfellow, I.; Bengio, Y.; and Courville, A. 2016. *Deep Learning*. MIT Press.
- Grathwohl, W.; Chen, R. T. Q.; Bettencourt, J.; Sutskever, I.; and Duvenaud, D. 2019. FFJORD: Free-Form Continuous Dynamics for Scalable Reversible Generative Models. In *7th International Conference on Learning Representations, ICLR 2019, New Orleans, LA, USA, May 6-9, 2019*.
- H. A. Dau; A. Bagnall; K. Kamgar; C. -C. M. Yeh; Y. Zhu; S. Gharghabi; C. A. Ratanamahatana; and E. Keogh. 2019. The UCR time series archive. *IEEE/CAA Journal of Automatica Sinica*, 6(6): 1293–1305.
- Horn, M.; Moor, M.; Bock, C.; Rieck, B.; and Borgwardt, K. 2020. Set Functions for Time Series. In III, H. D.; and Singh, A., eds., *Proceedings of the 37th International Conference on Machine Learning*, volume 119 of *Proceedings*

- of *Machine Learning Research*, 4353–4363. Proceedings of Machine Learning Research: PMLR.
- Hossain, T.; Ahad, M. A.; and Inoue, S. 2020. A Method for Sensor-Based Activity Recognition in Missing Data Scenario. *Sensors*, 20(14).
- Huang, C.-W.; Aghajohari, M.; Bose, J.; Panangaden, P.; and Courville, A. C. 2022. Riemannian Diffusion Models. In Koyejo, S.; Mohamed, S.; Agarwal, A.; Belgrave, D.; Cho, K.; and Oh, A., eds., *Advances in Neural Information Processing Systems*, volume 35, 2750–2761. Curran Associates, Inc.
- Hutchinson, M. 1989. A Stochastic Estimator of the Trace of the Influence Matrix for Laplacian Smoothing Splines. *Communications in Statistics - Simulation and Computation*, 18(3): 1059–1076.
- Ishikawa, I.; Teshima, T.; Tojo, K.; Oono, K.; Ikeda, M.; and Sugiyama, M. 2023. Universal Approximation Property of Invertible Neural Networks. *Journal of Machine Learning Research*, 24(287): 1–68.
- Jhin, S. Y.; Jo, M.; Kook, S.; and Park, N. 2023. Learnable Path in Neural Controlled Differential Equations. *Proceedings of the AAAI Conference on Artificial Intelligence*, 37(7): 8014–8022.
- Jhin, S. Y.; Lee, J.; Jo, M.; Kook, S.; Jeon, J.; Hyeong, J.; Kim, J.; and Park, N. 2022. EXIT: Extrapolation and Interpolation-based Neural Controlled Differential Equations for Time-series Classification and Forecasting. In *WWW '22: The ACM Web Conference 2022, Virtual Event, Lyon, France, April 25 - 29, 2022*, 3102–3112.
- Jhin, S. Y.; Shin, H.; Kim, S.; Hong, S.; Jo, M.; Park, S.; Park, N.; Lee, S.; Maeng, H.; and Jeon, S. 2024. Attentive neural controlled differential equations for time-series classification and forecasting. *Knowledge and Information Systems*, 66(3): 1885–1915.
- Ji, J.; Cao, Y.; Ma, Y.; and Yan, J. 2025. TITD: enhancing optimized temporal position encoding with time intervals and temporal decay in irregular time series forecasting. *Applied Intelligence*, 55(6): 415.
- Kapuśniak, K.; Potapchik, P.; Reu, T.; Zhang, L.; Tong, A.; Bronstein, M.; Bose, A. J.; and Di Giovanni, F. 2024. Metric Flow Matching for Smooth Interpolations on the Data Manifold. In Globerson, A.; Mackey, L.; Belgrave, D.; Fan, A.; Paquet, U.; Tomczak, J.; and Zhang, C., eds., *Advances in Neural Information Processing Systems*, volume 37, 135011–135042. Curran Associates, Inc.
- Kidger, P. 2022. On Neural Differential Equations.
- Kidger, P.; Morrill, J.; Foster, J.; and Lyons, T. J. 2020. Neural Controlled Differential Equations for Irregular Time Series. In *Advances in Neural Information Processing Systems 33: Annual Conference on Neural Information Processing Systems 2020, NeurIPS 2020, December 6-12, 2020, virtual*.
- Lechner, M.; and Hasani, R. 2020. Learning Long-Term Dependencies in Irregularly-Sampled Time Series.
- Li, Q.; Lin, T.; and Shen, Z. 2022. Deep learning via dynamical systems: An approximation perspective. *Journal of the European Mathematical Society*, 25(5): 1671–1709.
- Liaw, R.; Liang, E.; Nishihara, R.; Moritz, P.; Gonzalez, J. E.; and Stoica, I. 2018. Tune: A Research Platform for Distributed Model Selection and Training.
- Lin, H.; and Jegelka, S. 2018. ResNet with one-neuron hidden layers is a Universal Approximator. In *Advances in Neural Information Processing Systems 31: Annual Conference on Neural Information Processing Systems 2018, NeurIPS 2018, December 3-8, 2018, Montréal, Canada.*, 6172–6181.
- Lou, A.; Lim, D.; Katsman, I.; Huang, L.; Jiang, Q.; Lim, S. N.; and De Sa, C. M. 2020. Neural Manifold Ordinary Differential Equations. In Larochelle, H.; Ranzato, M.; Hadsell, R.; Balcan, M. F.; and Lin, H., eds., *Advances in Neural Information Processing Systems*, volume 33, 17548–17558. Curran Associates, Inc.
- Lu, Y.; Zhong, A.; Li, Q.; and Dong, B. 2018. Beyond Finite Layer Neural Networks: Bridging Deep Architectures and Numerical Differential Equations. In Dy, J.; and Krause, A., eds., *Proceedings of the 35th International Conference on Machine Learning*, volume 80 of *Proceedings of Machine Learning Research*, 3276–3285. PMLR.
- Löning, M.; Bagnall, A.; Ganesh, S.; Kazakov, V.; Lines, J.; and Király, F. J. 2019. sktime: A Unified Interface for Machine Learning with Time Series.
- Mathieu, E.; and Nickel, M. 2020. Riemannian Continuous Normalizing Flows. In Larochelle, H.; Ranzato, M.; Hadsell, R.; Balcan, M. F.; and Lin, H., eds., *Advances in Neural Information Processing Systems*, volume 33, 2503–2515. Curran Associates, Inc.
- Medsker, L.; and Jain, L. C. 1999. *Recurrent Neural Networks: Design and Applications*. CRC Press.
- Moritz, P.; Nishihara, R.; Wang, S.; Tumanov, A.; Liaw, R.; Liang, E.; Elibol, M.; Yang, Z.; Paul, W.; Jordan, M. I.; et al. 2018. Ray: a distributed framework for emerging AI applications. In *Proceedings of the 13th USENIX Conference on Operating Systems Design and Implementation, OSDI'18*, 561–577. USA: USENIX Association.
- Morrill, J.; Kidger, P.; Yang, L.; and Lyons, T. 2022. On the Choice of Interpolation Scheme for Neural CDEs. *Transactions on Machine Learning Research*.
- Morrill, J.; Salvi, C.; Kidger, P.; and Foster, J. 2021. Neural Rough Differential Equations for Long Time Series. In *Proceedings of the 38th International Conference on Machine Learning, ICML 2021, 18-24 July 2021, Virtual Event.*, 7829–7838.
- Oh, Y.; Kam, S.; Lee, J.; Lim, D.-Y.; Kim, S.; and Bui, A. 2025a. Comprehensive Review of Neural Differential Equations for Time Series Analysis.
- Oh, Y.; Lim, D.; and Kim, S. 2024. Stable Neural Stochastic Differential Equations in Analyzing Irregular Time Series Data. In *The Twelfth International Conference on Learning Representations, ICLR 2024, Vienna, Austria, May 7-11, 2024*. OpenReview.net.
- Oh, Y.; Lim, D.; Kim, S.; and Bui, A. A. T. 2025b. TANDEM: Temporal Attention-guided Neural Differential Equations for Missingness in Time Series Classification. In *Proceedings of the 34th ACM International Conference on In-*

- formation and Knowledge Management*, 2232–2242. Seoul, Republic of Korea: Association for Computing Machinery.
- Oh, Y.; Lim, D.-Y.; and Kim, S. 2025. DualDynamics: Synnergizing Implicit and Explicit Methods for Robust Irregular Time Series Analysis. In Walsh, T.; Shah, J.; and Kolter, Z., eds., *AAAI-25, Sponsored by the Association for the Advancement of Artificial Intelligence, February 25 - March 4, 2025, Philadelphia, PA, USA*, 19730–19739. AAAI Press.
- Papamakarios, G.; Nalisnick, E.; Rezende, D. J.; Mohamed, S.; and Lakshminarayanan, B. 2021. Normalizing Flows for Probabilistic Modeling and Inference. *Journal of Machine Learning Research*, 22(57): 1–64.
- Pollini, N.; Lavan, O.; and Amir, O. 2018. Adjoint sensitivity analysis and optimization of hysteretic dynamic systems with nonlinear viscous dampers. *Structural and Multidisciplinary Optimization*, 57(6): 2273–2289.
- Reyna, M. A.; Josef, C. S.; Jeter, R.; Shashikumar, S. P.; Westover, M. B.; Nemati, S.; Clifford, G. D.; and Sharma, A. 2020. Early Prediction of Sepsis From Clinical Data: The PhysioNet/Computing in Cardiology Challenge 2019. *Critical Care Medicine*, 48(2).
- Rubanova, Y.; Chen, T. Q.; and Duvenaud, D. 2019. Latent Ordinary Differential Equations for Irregularly-Sampled Time Series. In *Advances in Neural Information Processing Systems 32: Annual Conference on Neural Information Processing Systems 2019, NeurIPS 2019, December 8-14, 2019, Vancouver, BC, Canada.*, 5321–5331.
- S. Hochreiter; and J. Schmidhuber. 1997. Long Short-Term Memory. *Neural Computation*, 9(8): 1735–1780.
- Shukla, S. N.; and Marlin, B. M. 2019. Interpolation-Prediction Networks for Irregularly Sampled Time Series. In *7th International Conference on Learning Representations, ICLR 2019, New Orleans, LA, USA, May 6-9, 2019*.
- Shukla, S. N.; and Marlin, B. M. 2021. Multi-Time Attention Networks for Irregularly Sampled Time Series. In *9th International Conference on Learning Representations, ICLR 2021, Virtual Event, Austria, May 3-7, 2021*.
- Teshima, T.; Ishikawa, I.; Tojo, K.; Oono, K.; Ikeda, M.; and Sugiyama, M. 2020. Coupling-based Invertible Neural Networks Are Universal Diffeomorphism Approximators. In Larochelle, H.; Ranzato, M.; Hadsell, R.; Balcan, M. F.; and Lin, H., eds., *Advances in Neural Information Processing Systems*, volume 33, 3362–3373. Curran Associates, Inc.
- Vaswani, A.; Shazeer, N.; Parmar, N.; Uszkoreit, J.; Jones, L.; Gomez, A. N.; Kaiser, L.; and Polosukhin, I. 2017. Attention is All you Need. In Guyon, I.; Luxburg, U. V.; Bengio, S.; Wallach, H.; Fergus, R.; Vishwanathan, S.; and Garnett, R., eds., *Advances in Neural Information Processing Systems*, volume 30. Curran Associates, Inc.
- White, A.; Kilbertus, N.; Gelbrecht, M.; and Boers, N. 2023. Stabilized Neural Differential Equations for Learning Dynamics with Explicit Constraints. In Oh, A.; Naumann, T.; Globerson, A.; Saenko, K.; Hardt, M.; and Levine, S., eds., *Advances in Neural Information Processing Systems*, volume 36, 12929–12950. Curran Associates, Inc.
- Wu, Y.; Ni, J.; Cheng, W.; Zong, B.; Song, D.; Chen, Z.; Liu, Y.; Zhang, X.; Chen, H.; and Davidson, S. B. 2021. Dynamic Gaussian Mixture based Deep Generative Model For Robust Forecasting on Sparse Multivariate Time Series. *Proceedings of the AAAI Conference on Artificial Intelligence*, 35(1): 651–659.
- Wu, Z.; Pan, S.; Long, G.; Jiang, J.; Chang, X.; and Zhang, C. 2020. Connecting the Dots: Multivariate Time Series Forecasting with Graph Neural Networks. In *Proceedings of the 26th ACM SIGKDD International Conference on Knowledge Discovery & Data Mining*, 753–763. Virtual Event, CA, USA: Association for Computing Machinery.
- Xu, X.; Hasan, A.; Elkhilil, K.; Ding, J.; and Tarokh, V. 2023. Characteristic Neural Ordinary Differential Equation. In *The Eleventh International Conference on Learning Representations, ICLR 2023, Kigali, Rwanda, May 1-5, 2023*.
- Y. Wei; J. Peng; T. He; C. Xu; J. Zhang; S. Pan; and S. Chen. 2023. Compatible Transformer for Irregularly Sampled Multivariate Time Series. In *2023 IEEE International Conference on Data Mining (ICDM)*, 1409–1414.
- Zhang, X.; Zeman, M.; Tsiligkaridis, T.; and Zitnik, M. 2022. Graph-Guided Network for Irregularly Sampled Multivariate Time Series. In *The Tenth International Conference on Learning Representations, ICLR 2022, Virtual Event, April 25-29, 2022*.

Theoretical Considerations

This section provides expanded explanations and clarifications for the theoretical claims stated in the manuscript. We restate key assumptions where necessary and detail each step of the arguments.

Proof of Theorem 1

Proof. Fix $\theta = (\theta_f, \theta_F)$ and omit the explicit dependence on θ . Set

$$v(t, z) = f(t, z)\dot{\Phi}(t), \quad \text{where} \quad \dot{z}(t) = v(t, z(t)).$$

Since Φ is a C^1 diffeomorphism and f is Lipschitz in z , the vector field $v(t, z)$ is C^1 in z and continuous in t . By the continuity of Liouville equation, the density $p(z, t)$ satisfies

$$\frac{\partial p}{\partial t}(z, t) + \nabla_z \cdot (p(z, t) v(t, z)) = 0.$$

Along the solution $z(t)$, the total time-derivative of $\log p$ is

$$\begin{aligned} \frac{d}{dt} \log p(z(t), t) &= \frac{1}{p} \left(\frac{\partial p}{\partial t} + \dot{z}(t)^\top \nabla_z p \right) \\ &= -\frac{1}{p} \nabla_z \cdot (pv) = -\nabla_z \cdot v(t, z(t)). \end{aligned}$$

Substituting $v(t, z) = f(t, z)\dot{\Phi}(t)$ gives

$$\frac{d}{dt} \log p(z(t)) = -\operatorname{div}_z \left(f(t, z(t))\dot{\Phi}(t) \right),$$

Since v is C^1 in z over the compact domain $[0, T] \times \mathbb{R}^{d_z}$, its divergence is bounded. Hence the density cannot collapse to zero or blow up to infinity in finite time. \square

Proof of Theorem 2

Proof. Fix θ_f and θ_F , and omit explicit dependence on $\theta = (\theta_f, \theta_F)$. Recall the FlowPath integral equation

$$z(t) = z(0) + \int_0^t f(\tau, z(\tau); \theta_f)\dot{\Phi}(\tau; \theta_F) d\tau.$$

Define the combined vector field

$$v(t, z) = f(t, z; \theta_f)\dot{\Phi}(t; \theta_F).$$

Since $\Phi(\cdot; \theta_F)$ is C^1 on $[0, T]$, set

$$M_\Phi = \sup_{t \in [0, T]} \|\dot{\Phi}(t; \theta_F)\| < \infty.$$

By assumption, $f(t, \cdot; \theta_f)$ is L_f -Lipschitz in z , uniformly in t . Hence for any z_1, z_2 ,

$$\begin{aligned} \|v(t, z_1) - v(t, z_2)\| &= \|f(t, z_1)\dot{\Phi}(t) - f(t, z_2)\dot{\Phi}(t)\| \\ &\leq M_\Phi \|f(t, z_1) - f(t, z_2)\| \leq L_f M_\Phi \|z_1 - z_2\|. \end{aligned}$$

Thus $v(t, z)$ is Lipschitz in z and continuous in t . Applying the Picard–Lindelöf theorem to the ODE

$$\dot{z}(t) = v(t, z(t)), \quad z(0) = z_0,$$

we conclude there is a unique continuous solution $z(t)$ on $[0, T]$. \square

Proof of Theorem 3

Proof. Assume throughout that the time horizon $T > 0$ is fixed and finite, and assume that

$$\|f(t, z; \theta_f)\| \leq F_\infty \quad \text{for all } t \in [0, T], z \in \mathbb{R}^{d_z}.$$

Fix two parameter vectors $\theta_i = (\theta_{f,i}, \theta_{F,i})$ and write $z_i(t) = z_{\theta_i}(t)$ for $i = 1, 2$. Let

$$\Delta z(t) = z_1(t) - z_2(t), \quad \Delta \theta = (\Delta \theta_f, \Delta \theta_F) = (\theta_{f,1} - \theta_{f,2}, \theta_{F,1} - \theta_{F,2}).$$

By the FlowPath integral,

$$\Delta z(t) = \int_0^t \left[f(s, z_1(s); \theta_{f,1})\dot{\Phi}(s; \theta_{F,1}) - f(s, z_2(s); \theta_{f,2})\dot{\Phi}(s; \theta_{F,2}) \right] ds.$$

We add and subtract intermediate terms to split the integrand:

$$\begin{aligned} f_1 \dot{\Phi}_1 - f_2 \dot{\Phi}_2 &= [f_1 - f(s, \mathbf{z}_1; \theta_{f,2})] \dot{\Phi}_1 + f(s, \mathbf{z}_1; \theta_{f,2}) [\dot{\Phi}_1 - \dot{\Phi}_2] \\ &\quad + [f(s, \mathbf{z}_1; \theta_{f,2}) - f(s, \mathbf{z}_2; \theta_{f,2})] \dot{\Phi}_2, \end{aligned}$$

where $f_i = f(s, \mathbf{z}_i(s); \theta_{f,i})$ and $\dot{\Phi}_i = \dot{\Phi}(s; \theta_{F,i})$. Using

$$\|\dot{\Phi}_i\| \leq M_\Phi, \quad \|\dot{\Phi}_1 - \dot{\Phi}_2\| \leq L_\Phi \|\Delta\theta_F\|, \quad \|f(s, \mathbf{z}; \theta_{f,1}) - f(s, \mathbf{z}; \theta_{f,2})\| \leq L_\theta \|\Delta\theta_f\|,$$

and the Lipschitz constant L_f in \mathbf{z} , we get

$$\|\Delta\mathbf{z}(t)\| \leq (L_\theta M_\Phi + F_\infty L_\Phi) \|\Delta\theta\| t + L_f M_\Phi \int_0^t \|\Delta\mathbf{z}(s)\| ds.$$

By Grönwall's inequality, we confirm that \mathbf{z} is Lipschitz:

$$\|\Delta\mathbf{z}(T)\| \leq A \|\Delta\theta\|,$$

where $A := (L_\theta M_\Phi + F_\infty L_\Phi) T e^{L_f M_\Phi T}$. Since the loss \mathcal{L} is also ℓ -Lipschitz,

$$|\mathcal{L}(\mathbf{z}_1(T)) - \mathcal{L}(\mathbf{z}_2(T))| \leq \ell \|\Delta\mathbf{z}(T)\| \leq L \|\Delta\theta\|, \quad L = \ell A.$$

Thus \mathcal{F}_Θ is L -Lipschitz in θ . Now, we exactly follow the standard argument in (Bartlett, Foster, and Telgarsky 2017; Chen, Li, and Zhao 2020). If Θ has diameter D , covering-number arguments yield

$$\mathcal{N}(\mathcal{F}_\Theta, \eta) \leq \left(1 + \frac{LD}{\eta}\right)^d.$$

A Dudley-entropy-integral bound then shows

$$\text{Rad}(\mathcal{F}_\Theta) = \mathcal{O}\left(\frac{LD\sqrt{d}}{\sqrt{n}}\right) =: \kappa \frac{1}{\sqrt{n}}.$$

Finally, symmetrization and McDiarmid's concentration imply that, for any $\delta > 0$, with probability at least $1 - \delta$,

$$|\mathcal{R}_{\text{true}}(\hat{f}) - \mathcal{R}_{\text{emp}}(\hat{f})| \leq 2\text{Rad}(\mathcal{F}_\Theta) + \sqrt{\frac{\ln(1/\delta)}{2n}} \leq \alpha \frac{1}{\sqrt{n}} + \sqrt{\frac{\ln(1/\delta)}{2n}},$$

with $\alpha = 2\kappa$. This completes the proof. \square

Implementation details of FlowPath

Perspectives on NDEs' Robustness and Manifold Learning

FlowPath's contributions can advance two ongoing research thrusts in the NDE community: the development of robust models, and the integration of manifold learning to respect the intrinsic geometry of data.

One strategy for robust NDEs is to constrain the learned dynamics through physical or mathematical priors on the vector field f . For example, stability can be enforced via conservation laws (White et al. 2023), or by designing stable classes of stochastic systems to mitigate noise sensitivity (Oh, Lim, and Kim 2024), in the perspective of Neural Stochastic Differential Equations (Neural SDEs). Compared to that, FlowPath leaves the dynamics function f unconstrained and instead achieves robustness by imposing a strong structural prior on the control path $\Phi(t)$ itself. This regularizes the system by ensuring the data manifold that drives the dynamics is well-behaved, rather than by limiting the flexibility of the dynamics that evolve upon it.

Another active area focuses on learning the data manifold explicitly, moving beyond the Euclidean assumptions of standard NDEs. One approach constrains the dynamics to remain tangent to a learned manifold, as in Neural Manifold ODEs (Lou et al. 2020). Related advances in generative modeling apply continuous flows or diffusion processes on Riemannian manifolds (Mathieu and Nickel 2020; Huang et al. 2022), and recent work in metric flow matching emphasizes the importance of respecting intrinsic geometry (Chen and Lipman 2024; Kapuśniak et al. 2024). FlowPath shares this manifold-aware motivation but with a more modular design. Our method learns a data-driven manifold to define the control path, while the dynamics themselves evolve in the ambient space of the NDE. This decouples the learning of the geometric structure from the evolution rule.

These different philosophies highlight a trade-off between expressivity and structure. Models like Characteristic-Neural ODEs (Xu et al. 2023) are designed for maximum flexibility, enabling them to learn complex, non-homeomorphic transformations that can represent intersecting trajectories. In contrast, FlowPath intentionally leverages the structural constraint of a diffeomorphism as a powerful inductive bias. We posit that for robust classification from sparse observations, preserving the topology of the input data via an invertible map is a more beneficial constraint than allowing for arbitrary topological changes. This reflects a clear modeling choice, prioritizing a stable and well-behaved latent representation as the foundation for robust downstream performance.

Design of Flow Model

In our framework, the trainable control path $\Phi(t)$ is realized through an invertible mapping $F: [0, T] \times \mathbb{R}^{d_x} \rightarrow \mathbb{R}^{d_x}$ following Bilos et al. (2021). Building on classical results in dynamical systems, we ensure Φ maintains bijectivity and differentiability, preserving local volumes in the latent space. We implement three architecture choices:

ResNet Flow. Extending residual networks to continuous time (Chen et al. 2018), we define:

$$F(t, \mathbf{z}) = \mathbf{z} + \varphi(t) f(t, \mathbf{z}),$$

where φ encodes time dependence and f is a Lipschitz neural network. Invertibility follows from spectral normalization (Behrmann et al. 2019).

GRU Flow. Following Brouwer et al. (2019), we adapt the GRU architecture to continuous time:

$$F(t, \mathbf{z}) = \mathbf{z} + \varphi(t)(1 - f_1(t, \mathbf{z})) \odot (f_2(t, \mathbf{z}) - \mathbf{z}),$$

preserving memory capabilities while ensuring invertibility through careful gating constraints.

Coupling Flow. Inspired by normalizing flows (Dinh, Krueger, and Bengio 2015; Dinh, Sohl-Dickstein, and Bengio 2017), we partition \mathbf{z} and apply:

$$F(t)_{d_1} = \mathbf{z}_{d_1} \exp(u(t, \mathbf{z}_{d_2})\varphi_u(t)) + v(t, \mathbf{z}_{d_2})\varphi_v(t),$$

where $d_1 \cup d_2$ forms a complete partition, enabling efficient Jacobian computation.

We design our flow architecture to balance expressiveness with computational efficiency, guided by Papamakarios et al. (2021)’s normalizing-flow framework. In practice, we leverage Hutchinson’s trace estimator (Hutchinson 1989) for efficient Jacobian-related computations, further reducing the overhead of flow-based modeling (Grathwohl et al. 2019; Bilos et al. 2021; Oh, Lim, and Kim 2025). The flow architecture is designed to balance computational efficiency and representational expressiveness. We optimize its configuration during the tuning process and validate our choices through an ablation study.

Adjoint-sensitive method of FlowPath

The adjoint method is a powerful technique often used to calculate the gradients of systems governed by differential equations (Pollini, Lavan, and Amir 2018). The adjoint-sensitive method, proposed to solve Neural ODEs, reduces the memory requirements and computational burden that would otherwise be associated with backpropagating gradients through the solution of an ODE or CDE (Chen et al. 2018; Kidger et al. 2020). The primary concept of the adjoint-sensitive method is to introduce an adjoint state, usually denoted as $\mathbf{a}(t)$, which satisfies an auxiliary differential equation running backward in time. Algorithm 1 summarizes the procedure for performing the parameter update using the adjoint-sensitivity framework in FlowPath.

Algorithm 1: Adjoint-sensitivity method for FlowPath

- 1: Initialize parameters $\theta = \{\theta_f, \theta_F, \}, \theta_{\text{MLP}}$
- 2: **Forward:**
- 3: numerically solve Eq. (2) for $\mathbf{z}(t)$ over $t \in [0, T]$
- 4: Compute loss $\mathcal{L}(\text{MLP}(\mathbf{z}(T)); \theta_{\text{MLP}}, y)$
- 5: **Backward:**
- 6: (a) Set $\mathbf{a}(T) = \frac{\partial \mathcal{L}}{\partial \mathbf{z}(T)}$
- 7: (b) Numerically integrate backward ($t = T \rightarrow 0$)

$$\frac{d\mathbf{a}(t)}{dt} = -\mathbf{a}(t)^\top \frac{\partial}{\partial \mathbf{z}} \left(f(t, \mathbf{z}(t); \theta_f) \dot{\Phi}(t; \theta_F) \right),$$

- 8: (c) Compute

$$\frac{\partial \mathcal{L}}{\partial \theta} = \int_0^T \mathbf{a}(t)^\top \frac{\partial}{\partial \theta} \left[f(t, \mathbf{z}(t); \theta_f) \dot{\Phi}(t; \theta_F) \right] dt$$

- 9: **Update:** $\theta \leftarrow \theta - \eta \frac{\partial \mathcal{L}}{\partial \theta}$, where η is learning rate
 - 10: **Return:** θ
-

Denote all parameters collectively by $\theta = (\theta_f, \theta_F)$. Let \mathcal{L} be a scalar loss depending on $\mathbf{z}(T)$. Then, define an adjoint $\mathbf{a}(t) \in \mathbb{R}^{d_z}$ by integrating backward in time:

$$\frac{d\mathbf{a}(t)}{dt} = -\mathbf{a}(t)^\top \frac{\partial}{\partial \mathbf{z}} \left[f(t, \mathbf{z}(t); \theta_f) \dot{\Phi}(t; \theta_F) \right],$$

where $\mathbf{a}(T) = \frac{\partial \mathcal{L}}{\partial \mathbf{z}(T)}$. Solving this ODE backward ($t = T \rightarrow 0$) provides a continuous $\mathbf{a}(t)$ without needing to store all states $\{\mathbf{z}(t)\}$. Once $\mathbf{a}(t)$ is determined, the derivative of \mathcal{L} with respect to θ is

$$\frac{\partial \mathcal{L}}{\partial \theta} = \int_0^T \mathbf{a}(t)^\top \frac{\partial}{\partial \theta} \left[f(t, \mathbf{z}(t); \theta_f) \dot{\Phi}(t; \theta_F) \right] dt,$$

which also involves evaluating $\mathbf{z}(t)$ at certain query points. By avoiding explicit backprop through the entire forward trajectory, only the final state $\mathbf{z}(T)$ and the backward ODE for $\mathbf{a}(t)$ are integrated. This approach significantly reduces memory overhead for training large models or datasets.

Then, $\mathbf{z}(T)$ is fed into a multi-layer perceptron (MLP) classifier, and the cross-entropy loss is computed between the predicted label $\hat{y} = \text{MLP}(\mathbf{z}(T); \theta_{\text{MLP}})$ and the true label y .

Detailed results on time series classification with missingness

Experimental settings

The experiments were conducted on an Ubuntu 22.04 LTS server, which had an Intel(R) Xeon(R) Gold 6242 CPU and a cluster of NVIDIA A100 40GB GPUs. The source code for our experiments is available at <https://github.com/yongkyung-oh/FlowPath>.

Description of datasets. We performed classification experiments using 18 datasets spanning three distinct domains from the University of East Anglia (UEA) and the University of California Riverside (UCR) Time Series Classification Repository¹ (Bagnall et al. 2018; H. A. Dau et al. 2019). These experiments utilized the Python library `sktime` (Löning et al. 2019). As summarized in Table 8, datasets in the Sensor domain contain only univariate time series, while datasets in the other domains include both univariate and multivariate time series. To address the issue of varying sequence lengths, all time series were uniformly scaled to match the length of the longest sequence (Oh, Lim, and Kim 2024, 2025; Oh et al. 2025b). This scaling approach ensured consistent input dimensions across datasets for modeling.

After aligning the series lengths, random missing values, including 30%, 50%, and 70%, were introduced into each time series to simulate real-world scenarios. The datasets were then partitioned into training, validation, and testing subsets, using a ratio of 70%, 15%, and 15% respectively. Unlike the original splits from Bagnall et al. (2018), which varied across datasets, this partitioning ensured a uniform evaluation framework. Finally, the altered time series for each variable were integrated into a unified dataset. To evaluate model robustness, multiple cross-validation iterations were performed, each with a unique random seed for variability and statistical reliability.

Table 8: Description of datasets for the classification task

Domain	Dataset	Total number of samples	Number of classes	Dimension of time series	Length of time series
Motion & HAR	BasicMotions	80	4	6	100
	Epilepsy	275	4	3	206
	PickupGestureWiimoteZ	100	10	1	29-361
	ShakeGestureWiimoteZ	100	10	1	41-385
	ToeSegmentation1	268	2	1	277
	ToeSegmentation2	166	2	1	343
ECG & EEG	Blink	950	2	4	510
	ECG200	200	2	1	96
	SelfRegulationSCP1	561	2	6	896
	SelfRegulationSCP2	380	2	7	1152
	StandWalkJump	27	3	4	2500
	TwoLeadECG	1162	2	1	82
Sensor	DodgerLoopDay	158	7	1	288
	DodgerLoopGame	158	2	1	288
	DodgerLoopWeekend	158	2	1	288
	Lightning2	121	2	1	637
	Lightning7	143	7	1	319
	Trace	200	4	1	275

Training strategies. In every model and dataset, we seek to minimize the validation loss by optimizing the hyperparameters as suggested by Oh, Lim, and Kim (2024). The hyperparameters are optimized using the following scheme: Learning rate $\eta \in \{10^{-4}, 10^{-1}\}$, sampled from a log-uniform distribution; Number of layers $n_l \in \{1, 2, 3, 4\}$, determined via grid search;

¹<http://www.timeseriesclassification.com/>

Hidden vector dimensions $n_h \in \{16, 32, 64, 128\}$, selected through grid search; Batch size chosen from $\{16, 32, 64, 128\}$, adjusted according to the total data size.

It is important that for the sake of fairness and integrity in comparative analysis, we employed the original source code provided by the authors of the aforementioned models. In regard to hyperparameter tuning, we undertook a systematic approach for each model and dataset. This was facilitated by the employment of the Python library `ray`² (Moritz et al. 2018; Liaw et al. 2018). The hyperparameters were calibrated based on the original dataset, and the same configuration was consistently applied to scenarios incorporating missing data, ensuring consistency in experimental settings.

For RNN-based methods, these hyperparameters are used in the fully-connected layer, while for NDE-based methods, they are employed in the embedding layer and vector fields. Furthermore, Euler or Euler–Maruyama method is used to solve NDE-based methods. In case of the Neural Flow and the proposed FlowPath, three different flow models are considered with original source code³. As suggested in Bilos et al. (2021), we optimize the best flow model for each dataset. Also, we compare the performance of the different flow models in the ablation study. Each model undergoes training for a total of 100 epochs, with the best-performing model selected based on the lowest validation loss. The early-stopping is applied when the loss does not improve for 10 consecutive epochs.

Comparative Results with different domains

To ensure a comprehensive evaluation of our approach and to facilitate fair comparison with existing methods, we reproduce and extend the full benchmark suite with 18 datasets in three domains. This includes conducting experiments across all three major domains—Motion & Human Activity Recognition (HAR), Electrocardiogram (ECG) & Electroencephalogram (EEG), and various real-world datasets—spanning a total of 18 publicly available datasets. By aligning with this established benchmark, we aim to demonstrate the generalizability and robustness of our method across heterogeneous time series modalities.

Methods	Regular		30% Missing		50% Missing		70% Missing		Average	
	Accuracy	Rank	Accuracy	Rank	Accuracy	Rank	Accuracy	Rank	Accuracy	Rank
RNN	0.560 (0.072)	10.7	0.484 (0.075)	13.3	0.471 (0.082)	12.9	0.453 (0.068)	13.3	0.492 (0.074)	12.6
LSTM	0.588 (0.067)	10.0	0.552 (0.075)	9.4	0.516 (0.073)	10.5	0.505 (0.067)	10.6	0.540 (0.071)	10.1
GRU	0.674 (0.080)	6.9	0.639 (0.065)	8.0	0.611 (0.076)	8.2	0.606 (0.088)	8.1	0.633 (0.077)	7.8
GRU- Δt	0.629 (0.065)	9.1	0.636 (0.069)	7.6	0.651 (0.068)	6.7	0.649 (0.074)	7.5	0.641 (0.069)	7.7
GRU-D	0.593 (0.088)	10.0	0.579 (0.087)	9.8	0.580 (0.075)	9.7	0.599 (0.062)	9.4	0.588 (0.078)	9.7
GRU-ODE	0.663 (0.072)	7.2	0.661 (0.069)	6.8	0.664 (0.069)	6.5	0.659 (0.081)	6.3	0.662 (0.073)	6.7
ODE-RNN	0.652 (0.085)	6.8	0.632 (0.076)	7.3	0.626 (0.086)	7.2	0.653 (0.059)	5.8	0.641 (0.076)	6.8
ODE-LSTM	0.566 (0.074)	10.4	0.518 (0.069)	11.4	0.501 (0.068)	12.1	0.474 (0.068)	12.3	0.515 (0.070)	11.5
Neural CDE	0.681 (0.073)	7.1	0.672 (0.068)	7.3	0.661 (0.070)	7.0	0.652 (0.091)	7.0	0.667 (0.075)	7.1
Neural RDE	0.649 (0.082)	7.9	0.648 (0.071)	6.9	0.633 (0.078)	7.7	0.607 (0.079)	8.2	0.634 (0.078)	7.7
ANCDE	0.662 (0.083)	7.3	0.661 (0.083)	6.8	0.639 (0.080)	7.6	0.631 (0.073)	7.1	0.649 (0.080)	7.2
EXIT	0.595 (0.087)	9.4	0.580 (0.088)	9.8	0.578 (0.086)	9.5	0.564 (0.072)	10.0	0.579 (0.083)	9.7
LEAP	0.490 (0.062)	13.1	0.459 (0.070)	13.7	0.466 (0.074)	12.4	0.451 (0.074)	12.7	0.466 (0.070)	13.0
DualDynamics	<u>0.724 (0.090)</u>	<u>4.6</u>	<u>0.720 (0.088)</u>	<u>4.9</u>	<u>0.691 (0.091)</u>	<u>4.9</u>	<u>0.697 (0.098)</u>	<u>4.6</u>	<u>0.708 (0.092)</u>	<u>4.8</u>
Neural Flow	0.530 (0.069)	11.8	0.531 (0.072)	9.9	0.537 (0.073)	9.4	0.535 (0.082)	9.7	0.533 (0.074)	10.2
FlowPath	0.731 (0.083)	3.7	0.743 (0.091)	3.1	0.726 (0.084)	3.6	0.718 (0.090)	3.5	0.730 (0.087)	3.5

Settings	Regular	30% Missing	50% Missing	70% Missing	Average
Neural CDE	0.681 (0.073)	0.672 (0.068)	0.661 (0.070)	0.652 (0.091)	0.667 (0.075)
+ MLP	0.705 (0.077)	0.700 (0.084)	0.695 (0.091)	0.655 (0.084)	0.689 (0.084)
FlowPath	0.731 (0.083)	0.743 (0.091)	0.726 (0.084)	0.718 (0.090)	0.730 (0.087)
with ResNet Flow	0.705 (0.077)	0.724 (0.081)	0.697 (0.084)	0.693 (0.070)	0.705 (0.078)
with GRU Flow	0.715 (0.087)	0.713 (0.076)	0.701 (0.065)	0.681 (0.080)	0.702 (0.077)
with Coupling Flow	0.713 (0.085)	0.720 (0.084)	0.708 (0.084)	0.691 (0.100)	0.708 (0.088)

Table 9: Classification accuracy across all three domains, and the average results for all benchmarks and ablations.

Table 9 summarizes performance across all 18 datasets. Table 10 reports results on Motion & HAR datasets, Table 11 covers ECG & EEG datasets, and Table 12 presents results for Sensor datasets. Through these experiments, we perform a comprehensive comparison between FlowPath and several benchmark methods, and further conduct an ablation study to examine the specific impact and contribution of the flow-based modeling component within the overall FlowPath framework.

²<https://github.com/ray-project/ray>

³<https://github.com/mbilos/neural-flows-experiments>

Methods	Regular		30% Missing		50% Missing		70% Missing		Average	
	Accuracy	Rank	Accuracy	Rank	Accuracy	Rank	Accuracy	Rank	Accuracy	Rank
RNN	0.518 (0.062)	11.8	0.445 (0.077)	14.3	0.427 (0.061)	14.3	0.415 (0.070)	13.6	0.451 (0.067)	13.5
LSTM	0.568 (0.089)	10.3	0.522 (0.092)	10.8	0.494 (0.094)	11.1	0.467 (0.090)	12.5	0.513 (0.091)	11.2
GRU	0.696 (0.095)	7.0	0.629 (0.076)	9.6	0.612 (0.089)	8.7	0.631 (0.111)	7.3	0.642 (0.093)	8.1
GRU- Δt	0.613 (0.076)	8.2	0.624 (0.079)	7.0	0.663 (0.064)	6.6	0.624 (0.077)	9.0	0.631 (0.074)	7.7
GRU-D	0.587 (0.077)	10.3	0.563 (0.089)	10.4	0.540 (0.056)	12.0	0.564 (0.054)	10.3	0.563 (0.069)	10.8
GRU-ODE	0.662 (0.081)	8.1	0.647 (0.091)	8.8	0.656 (0.072)	8.2	0.657 (0.084)	6.7	0.656 (0.082)	7.9
ODE-RNN	0.621 (0.087)	9.0	0.603 (0.078)	8.0	0.588 (0.095)	8.1	0.627 (0.064)	6.9	0.610 (0.081)	8.0
ODE-LSTM	0.550 (0.083)	11.5	0.507 (0.080)	11.2	0.475 (0.102)	12.4	0.426 (0.094)	12.3	0.489 (0.089)	11.8
Neural CDE	<u>0.751 (0.096)</u>	5.3	<u>0.728 (0.080)</u>	5.4	0.717 (0.100)	5.6	<u>0.738 (0.111)</u>	5.7	<u>0.733 (0.097)</u>	5.5
Neural RDE	0.702 (0.091)	5.8	0.703 (0.077)	5.7	0.704 (0.088)	6.0	0.665 (0.095)	7.1	0.693 (0.088)	6.1
ANCDE	0.710 (0.068)	<u>5.0</u>	0.716 (0.075)	<u>4.7</u>	<u>0.724 (0.074)</u>	<u>3.8</u>	0.703 (0.077)	5.0	0.713 (0.074)	<u>4.6</u>
EXIT	0.548 (0.086)	9.7	0.584 (0.073)	8.5	0.567 (0.086)	9.5	0.534 (0.097)	10.8	0.558 (0.086)	9.6
LEAP	0.397 (0.084)	14.2	0.374 (0.086)	14.5	0.381 (0.077)	12.9	0.335 (0.062)	13.5	0.372 (0.077)	13.8
DualDynamics	0.704 (0.082)	5.8	0.702 (0.074)	5.3	0.696 (0.088)	4.8	0.723 (0.123)	<u>3.6</u>	0.706 (0.092)	4.8
Neural Flow	0.498 (0.082)	10.3	0.502 (0.085)	10.2	0.504 (0.081)	9.7	0.516 (0.093)	9.3	0.505 (0.085)	9.9
FlowPath	0.770 (0.079)	3.8	0.799 (0.080)	1.8	0.774 (0.092)	2.6	0.782 (0.094)	2.5	0.781 (0.086)	2.6

Settings	Regular	30% Missing	50% Missing	70% Missing	Average
Neural CDE	0.751 (0.096)	0.728 (0.080)	0.717 (0.100)	0.738 (0.111)	0.733 (0.097)
+ MLP	0.737 (0.114)	0.744 (0.105)	0.749 (0.110)	0.707 (0.111)	0.734 (0.110)
FlowPath	0.770 (0.079)	0.799 (0.080)	0.774 (0.092)	0.782 (0.094)	0.781 (0.086)
with ResNet Flow	0.762 (0.073)	0.794 (0.074)	0.761 (0.092)	0.768 (0.078)	0.771 (0.079)
with GRU Flow	0.775 (0.080)	0.776 (0.081)	0.765 (0.075)	0.775 (0.090)	0.773 (0.082)
with Coupling Flow	0.761 (0.073)	0.748 (0.075)	0.758 (0.068)	0.758 (0.085)	0.756 (0.075)

Table 10: Classification accuracy across ‘Motion & HAR’ domains, and the average results for all benchmarks and ablations.

Methods	Regular		30% Missing		50% Missing		70% Missing		Average	
	Accuracy	Rank	Accuracy	Rank	Accuracy	Rank	Accuracy	Rank	Accuracy	Rank
RNN	0.604 (0.075)	8.8	0.532 (0.058)	12.6	0.545 (0.062)	11.3	0.506 (0.056)	13.0	0.547 (0.063)	11.4
LSTM	0.609 (0.054)	9.8	0.592 (0.066)	7.7	0.568 (0.057)	8.9	0.546 (0.048)	9.2	0.579 (0.056)	8.9
GRU	0.692 (0.073)	5.0	<u>0.704 (0.059)</u>	<u>5.3</u>	0.658 (0.068)	7.4	0.661 (0.068)	6.8	0.679 (0.067)	6.1
GRU- Δt	0.602 (0.047)	11.3	0.616 (0.052)	9.6	0.624 (0.062)	7.8	0.616 (0.069)	9.0	0.614 (0.057)	9.4
GRU-D	0.621 (0.056)	8.8	0.606 (0.066)	9.8	0.618 (0.055)	9.0	0.585 (0.061)	10.9	0.608 (0.060)	9.6
GRU-ODE	0.650 (0.057)	7.8	0.661 (0.057)	6.3	0.653 (0.063)	7.3	0.633 (0.080)	7.6	0.649 (0.064)	7.2
ODE-RNN	0.664 (0.068)	5.6	0.650 (0.050)	6.7	0.644 (0.048)	8.2	0.647 (0.050)	<u>5.2</u>	0.651 (0.054)	6.4
ODE-LSTM	0.580 (0.058)	8.5	0.546 (0.065)	10.9	0.550 (0.054)	11.8	0.545 (0.036)	11.7	0.555 (0.053)	10.7
Neural CDE	0.643 (0.040)	7.9	0.632 (0.038)	8.4	0.625 (0.041)	8.4	0.596 (0.069)	7.8	0.624 (0.047)	8.1
Neural RDE	0.591 (0.065)	11.3	0.621 (0.060)	7.6	0.602 (0.070)	8.8	0.577 (0.073)	8.9	0.598 (0.067)	9.1
ANCDE	0.617 (0.075)	8.8	0.612 (0.060)	9.1	0.596 (0.059)	10.2	0.590 (0.072)	7.7	0.604 (0.066)	8.9
EXIT	0.599 (0.092)	10.2	0.552 (0.084)	11.4	0.563 (0.092)	10.8	0.574 (0.044)	9.8	0.572 (0.078)	10.5
LEAP	0.572 (0.051)	11.4	0.527 (0.080)	12.9	0.546 (0.093)	10.9	0.540 (0.086)	11.5	0.546 (0.077)	11.7
DualDynamics	0.708 (0.119)	<u>4.2</u>	0.747 (0.086)	5.7	<u>0.703 (0.086)</u>	<u>4.8</u>	<u>0.683 (0.096)</u>	6.0	0.710 (0.097)	<u>5.2</u>
Neural Flow	0.547 (0.061)	13.4	0.572 (0.061)	8.4	0.586 (0.080)	7.3	0.582 (0.087)	7.3	0.572 (0.072)	9.1
FlowPath	<u>0.698 (0.056)</u>	3.2	0.701 (0.090)	3.7	0.711 (0.076)	3.1	0.692 (0.085)	3.7	<u>0.701 (0.077)</u>	3.4

Settings	Regular	30% Missing	50% Missing	70% Missing	Average
Neural CDE	0.643 (0.040)	0.632 (0.038)	0.625 (0.041)	0.596 (0.069)	0.624 (0.047)
+ MLP	0.654 (0.049)	0.664 (0.068)	0.666 (0.087)	0.631 (0.045)	0.654 (0.062)
FlowPath	0.698 (0.056)	0.701 (0.090)	0.711 (0.076)	0.692 (0.085)	0.701 (0.077)
with ResNet Flow	0.679 (0.054)	0.688 (0.068)	0.681 (0.072)	0.667 (0.058)	0.679 (0.063)
with GRU Flow	0.665 (0.073)	0.671 (0.069)	0.675 (0.052)	0.637 (0.070)	0.662 (0.066)
with Coupling Flow	0.670 (0.075)	0.676 (0.084)	0.676 (0.092)	0.668 (0.111)	0.673 (0.090)

Table 11: Classification accuracy across ‘ECG & EEG’ domains, and the average results for all benchmarks and ablations.

Methods	Regular		30% Missing		50% Missing		70% Missing		Average	
	Accuracy	Rank	Accuracy	Rank	Accuracy	Rank	Accuracy	Rank	Accuracy	Rank
RNN	0.557 (0.078)	11.6	0.476 (0.089)	13.1	0.441 (0.123)	13.2	0.437 (0.079)	13.4	0.478 (0.092)	12.8
LSTM	0.588 (0.059)	10.0	0.542 (0.067)	9.8	0.484 (0.069)	11.5	0.503 (0.065)	10.1	0.529 (0.065)	10.3
GRU	0.633 (0.073)	8.8	0.585 (0.059)	9.2	0.563 (0.072)	8.4	0.526 (0.084)	10.0	0.577 (0.072)	9.1
GRU- Δt	0.673 (0.072)	7.8	0.666 (0.075)	6.1	0.668 (0.080)	5.6	0.708 (0.075)	4.5	0.679 (0.076)	6.0
GRU-D	0.569 (0.130)	10.8	0.569 (0.105)	9.3	0.583 (0.115)	8.1	0.647 (0.070)	6.8	0.592 (0.105)	8.7
GRU-ODE	0.677 (0.079)	5.8	0.674 (0.059)	<u>5.3</u>	<u>0.684 (0.072)</u>	4.0	<u>0.687 (0.079)</u>	4.7	0.680 (0.072)	4.9
ODE-RNN	0.673 (0.098)	5.8	0.642 (0.101)	7.2	0.647 (0.115)	5.3	0.684 (0.062)	5.3	0.662 (0.094)	5.9
ODE-LSTM	0.567 (0.083)	11.1	0.502 (0.061)	12.2	0.479 (0.049)	12.2	0.453 (0.075)	12.9	0.500 (0.067)	12.1
Neural CDE	0.650 (0.082)	8.0	0.657 (0.087)	7.9	0.641 (0.069)	7.1	0.623 (0.094)	7.5	0.643 (0.083)	7.6
Neural RDE	0.653 (0.089)	6.7	0.620 (0.076)	7.3	0.594 (0.077)	8.4	0.580 (0.069)	8.7	0.612 (0.078)	7.8
ANCDE	0.660 (0.106)	8.0	0.656 (0.115)	6.7	0.598 (0.108)	9.0	0.601 (0.069)	8.7	0.629 (0.100)	8.1
EXIT	0.637 (0.082)	8.3	0.605 (0.107)	9.5	0.606 (0.081)	8.3	0.584 (0.074)	9.3	0.608 (0.086)	8.9
LEAP	0.500 (0.052)	13.8	0.475 (0.044)	13.7	0.471 (0.054)	13.5	0.478 (0.073)	13.0	0.481 (0.056)	13.5
DualDynamics	0.760 (0.070)	4.0	<u>0.712 (0.106)</u>	3.9	0.673 (0.100)	<u>5.0</u>	<u>0.687 (0.076)</u>	4.3	0.708 (0.088)	4.3
Neural Flow	0.546 (0.065)	11.5	0.520 (0.071)	11.2	0.521 (0.058)	11.3	0.507 (0.068)	12.4	0.524 (0.065)	11.6
FlowPath	<u>0.726 (0.116)</u>	<u>4.2</u>	0.729 (0.103)	3.9	0.693 (0.085)	5.2	0.679 (0.092)	<u>4.4</u>	<u>0.707 (0.099)</u>	<u>4.4</u>

Settings	Regular	30% Missing	50% Missing	70% Missing	Average
Neural CDE	0.650 (0.082)	0.657 (0.087)	0.641 (0.069)	0.623 (0.094)	0.643 (0.083)
+ MLP	0.723 (0.069)	0.691 (0.079)	0.668 (0.076)	0.626 (0.097)	0.677 (0.080)
FlowPath	0.726 (0.116)	0.729 (0.103)	0.693 (0.085)	0.679 (0.092)	0.707 (0.099)
with ResNet Flow	0.675 (0.104)	0.690 (0.100)	0.647 (0.087)	0.646 (0.075)	0.664 (0.091)
with GRU Flow	0.704 (0.107)	0.692 (0.077)	0.664 (0.069)	0.631 (0.078)	0.673 (0.083)
with Coupling Flow	0.707 (0.108)	0.736 (0.092)	0.690 (0.094)	0.647 (0.105)	0.695 (0.100)

Table 12: Classification accuracy across ‘Sensor’ domains, and the average results for all benchmarks and ablations.

Pairwise Statistical Test. We perform pairwise comparisons between FlowPath and each baseline model across four missingness levels, as well as an aggregated setting that includes all levels. Statistical tests use one-sided Wilcoxon signed-rank tests (Demšar 2006), with Holm-Bonferroni adjustment for multiple comparisons (Giacalone et al. 2018). Significance is determined at the adjusted threshold of $p < 0.05$ (Benavoli, Corani, and Mangili 2016).

Methods	Regular	30% Missing	50% Missing	70% Missing	All Settings
RNN	16/0/2(*)	18/0/0(*)	18/0/0(*)	18/0/0(*)	70/0/2(*)
LSTM	16/0/2(*)	17/0/1(*)	17/0/1(*)	18/0/0(*)	68/0/4(*)
GRU	12/0/6	14/0/4(*)	13/0/5(*)	14/0/4	53/0/19(*)
GRU- Δt	13/0/5	13/2/3(*)	12/1/5	11/2/5	49/5/18(*)
GRU-D	16/0/2(*)	16/1/1(*)	15/0/3(*)	13/1/4(*)	60/2/10(*)
GRU-ODE	13/1/4(*)	12/0/6(*)	12/1/5	11/0/7	48/2/22(*)
ODE-RNN	15/0/3	13/1/4(*)	12/0/6	10/0/8	50/1/21(*)
ODE-LSTM	17/0/1(*)	17/1/0(*)	18/0/0(*)	17/0/1(*)	69/1/2(*)
Neural CDE	12/1/5	16/1/1(*)	13/1/4(*)	16/0/2(*)	57/3/12(*)
Neural RDE	15/0/3(*)	15/0/3(*)	14/1/3(*)	17/0/1(*)	61/1/10(*)
ANCDE	13/2/3(*)	15/1/2(*)	15/2/1(*)	17/0/1(*)	60/5/7(*)
EXIT	18/0/0(*)	17/0/1(*)	16/0/2(*)	17/0/1(*)	68/0/4(*)
LEAP	18/0/0(*)	18/0/0(*)	17/0/1(*)	17/0/1(*)	70/0/2(*)
DualDynamics	8/2/8	11/1/6	11/2/5	10/1/7	40/6/26(*)
Neural Flow	16/1/1(*)	16/0/2(*)	16/0/2(*)	16/1/1(*)	64/2/6(*)

Table 13: Pairwise comparison of FlowPath against all baselines across missing rates using Wilcoxon signed-rank tests

In Table 13, we report the number of datasets where FlowPath significantly outperforms (Wins), performs comparably (Ties), or underperforms (Losses) relative to the baseline, based on average results over five independent runs. Across all conditions, FlowPath demonstrates consistent advantages, with statistically significant improvements in most cases. These trends are maintained even under severe levels of missing data, suggesting that FlowPath effectively captures the underlying structure of partially observed time series. The overall results highlight the robustness and generalization benefits introduced by the proposed invertible manifold learning framework.

Comprehensive analysis of FlowPath

Showcase of FlowPath’s Learned Path. Figure 8, 9, 10, and 11 present multiple examples, which are randomly chosen from the test set, demonstrating the effectiveness of FlowPath in handling missing data. Our goal is not reconstructing the missing values but learning a more meaningful representation that benefits downstream tasks, particularly time series classification.

Each row corresponds to a different instance from the ‘BasicMotions’ dataset with a 50% missing rate. Given the highly irregular raw observations (a), a standard non-invertible MLP (b) learns a chaotic and unstructured path, suggesting it has overfit to the sparse points without capturing the true underlying dynamics. In contrast, the path learned by FlowPath (c) is visibly more stable and well-structured, reflecting the inductive bias of the invertible flow toward dynamically plausible manifolds.

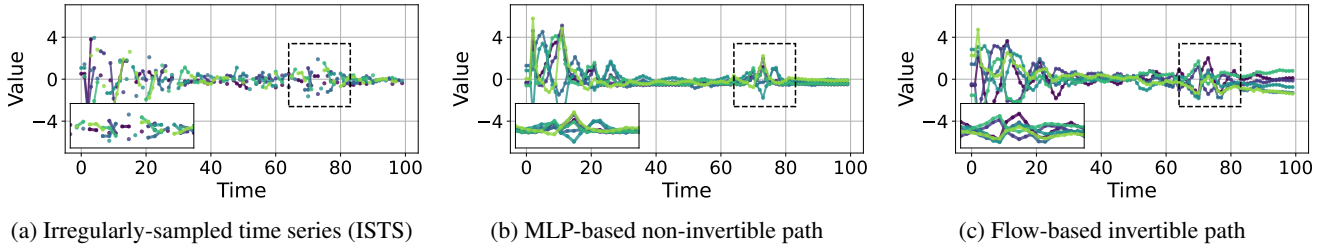


Figure 8: Continuous-time modeling through FlowPath (‘BasicMotions’ dataset, instance 1)

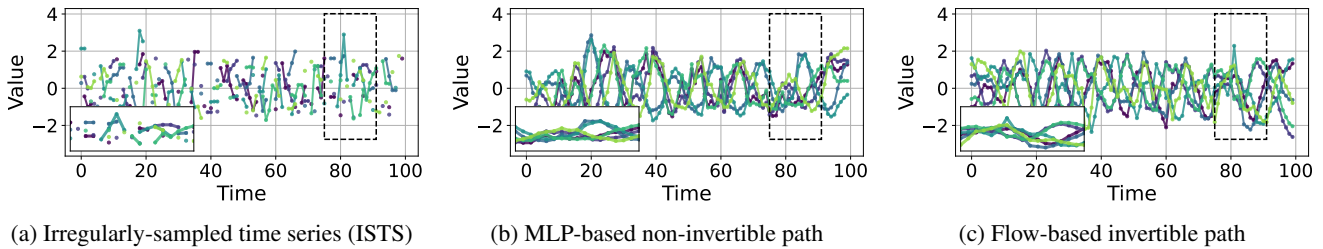


Figure 9: Continuous-time modeling through FlowPath (‘BasicMotions’ dataset, instance 2)

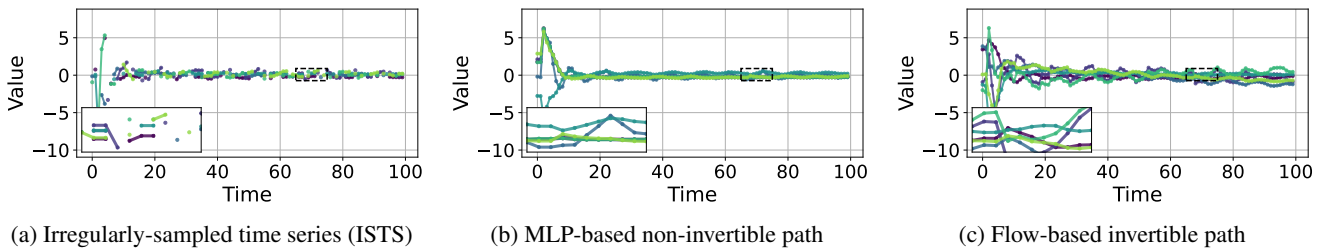


Figure 10: Continuous-time modeling through FlowPath (‘BasicMotions’ dataset, instance 3)

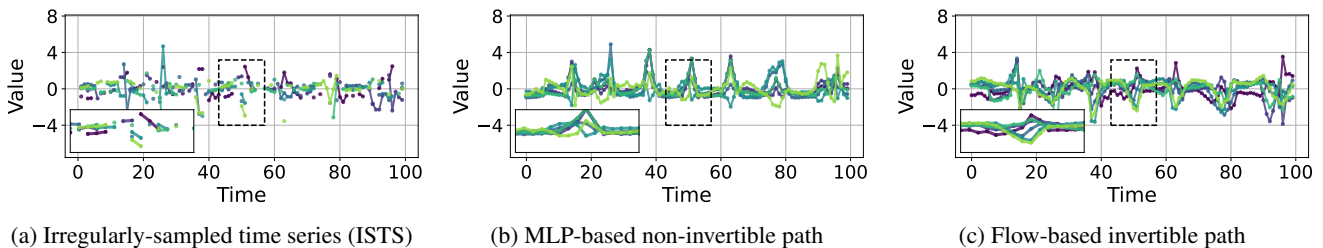


Figure 11: Continuous-time modeling through FlowPath (‘BasicMotions’ dataset, instance 4)

Detailed Qualitative Visualization of Learned Manifolds. To assess the structure of the learned representations, we analyze the trajectories and distributions on the ‘BasicMotions’ dataset with 50% missingness. Figure 12 visualizes 2D trajectories to assess geometric alignment, while Figure 13 shows 1D and 2D kernel density estimates to compare distributional overlap.

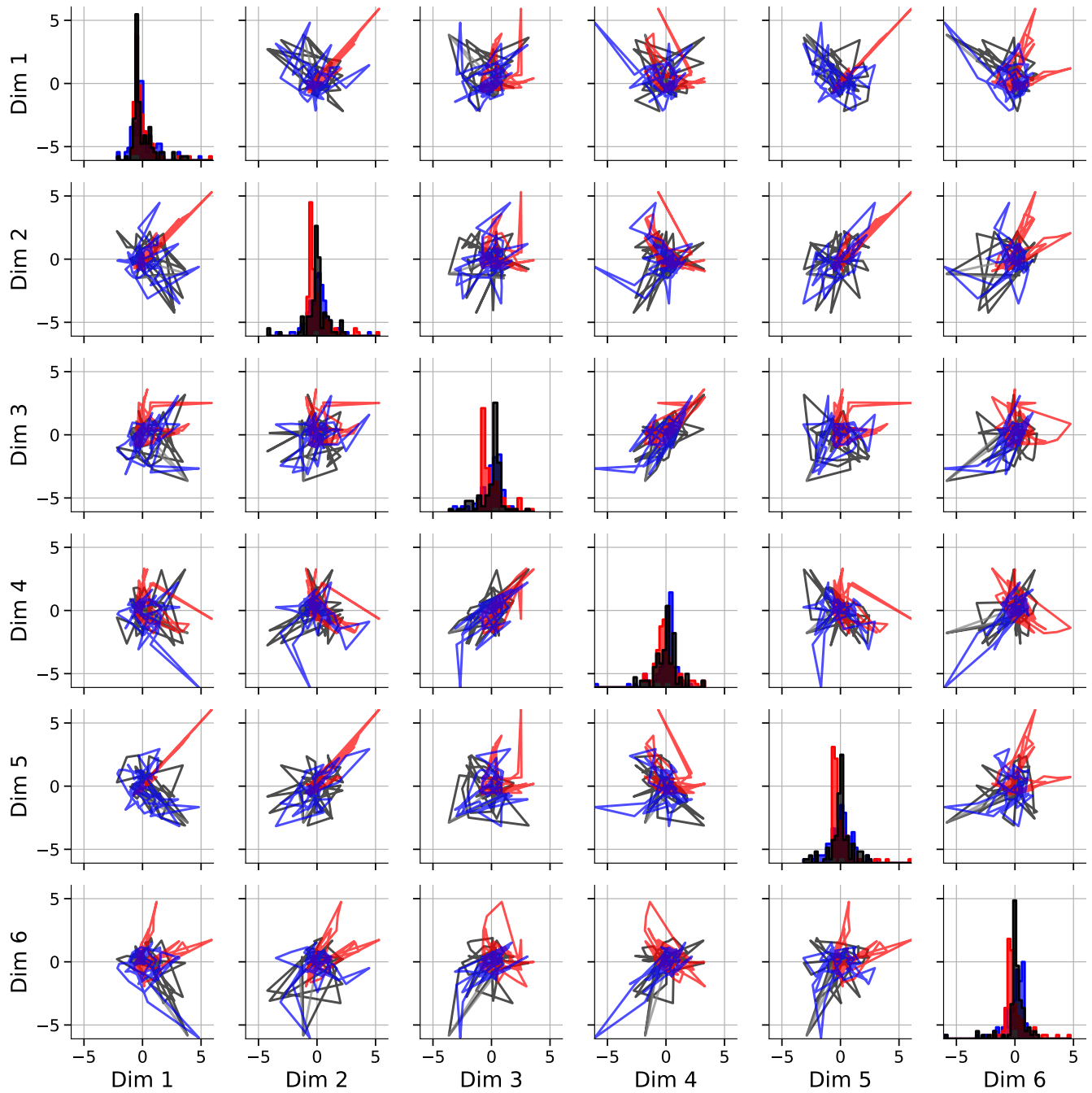


Figure 12: Learned manifolds visualized as 2D trajectories. Off-diagonal plots show phase-space paths, while diagonal plots display marginal histograms. The missing observation (gray) lacks dynamical information due to irregular sampling. The MLP path (red) deviates from the original geometry (black) and exhibits erratic behavior, suggesting overfitting to sparse inputs. In contrast, FlowPath (blue) more consistently captures the global structure and density of the original path. These differences highlight the role of invertibility in promoting stable and coherent representations under data sparsity.

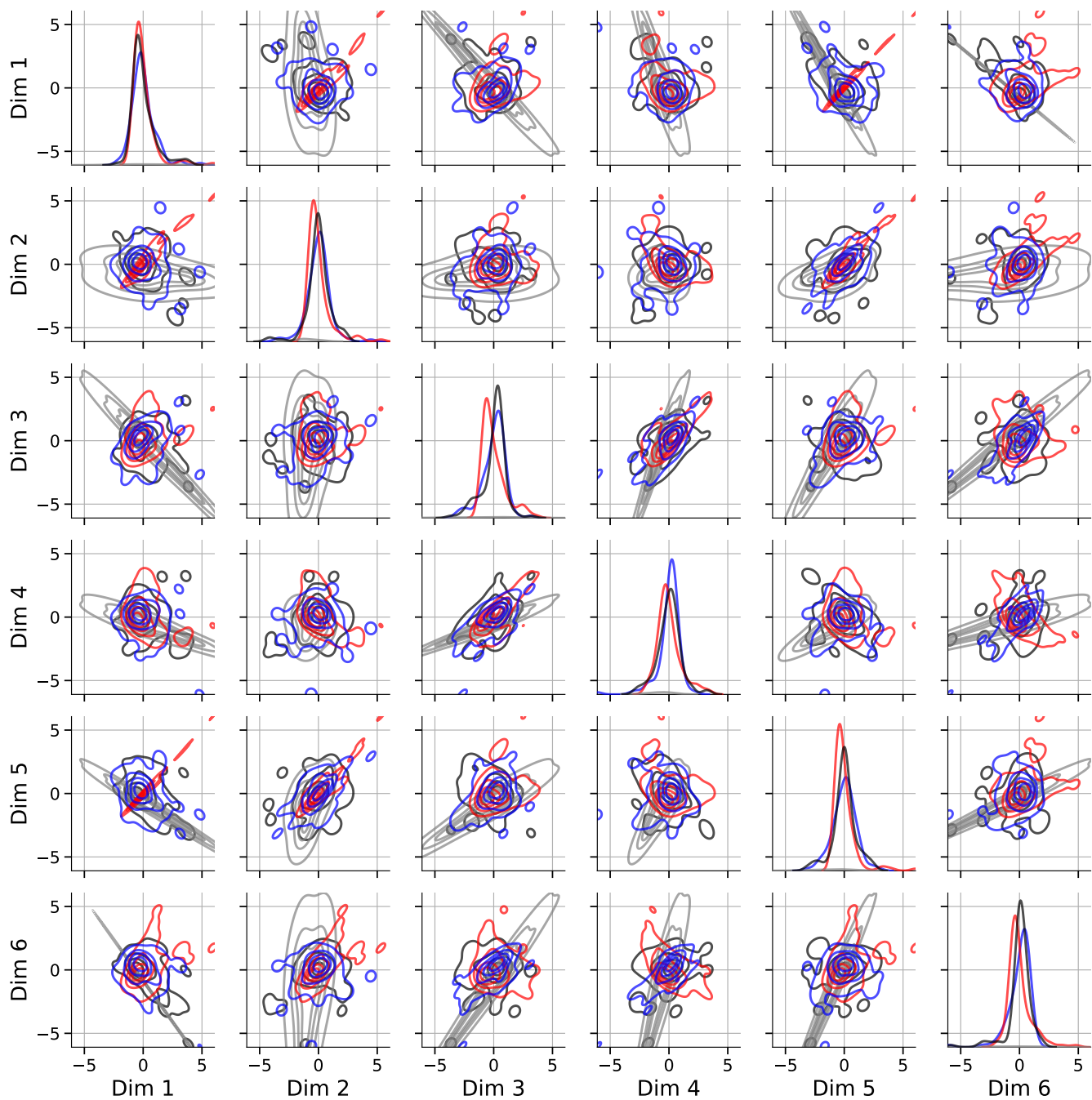


Figure 13: 1D and 2D kernel density estimates of the learned manifolds. FlowPath (blue) shows greater overlap with the original distribution (black) than the sparse observations (gray) and the MLP (red). The sparse observations are diffuse, and the MLP yields a distribution that diverges from the ground truth. In contrast, FlowPath exhibits closer alignment with the target density across projection spaces. While this does not imply full recovery of the underlying distribution, it indicates that FlowPath better approximates its underlying structure under sparse sampling.

Detailed results on real-world dataset with sensor dropout

The PAMAP2 dataset (A. Reiss and D. Stricker 2012)⁴ contains daily activity data from nine individuals, recorded using three inertial measurement units (placed on the wrist, chest, and ankle) and a heart rate monitor. To evaluate model robustness under sensor dropout scenarios, we adapted this dataset following the preprocessing method proposed by Zhang et al. (2022)⁵.

n_l	n_h	Neural CDE		FlowPath		
		Spline	MLP	ResNet	GRU	Coupling
1	16	35.9 ±0.6	83.0 ±1.0	56.6 ±5.1	49.3 ±3.0	42.0 ±1.2
	32	45.1 ±2.2	86.0 ±1.0	57.6 ±1.8	58.4 ±3.2	59.2 ±2.3
	64	52.6 ±3.2	87.8 ±0.3	68.1 ±2.4	69.3 ±3.0	66.7 ±1.6
	128	64.5 ±3.0	88.0 ±0.8	78.4 ±2.7	77.6 ±1.5	76.0 ±4.5
2	16	45.1 ±5.3	81.8 ±2.4	77.1 ±1.5	73.7 ±1.5	68.4 ±0.5
	32	61.1 ±6.0	86.0 ±0.3	81.6 ±3.0	75.5 ±0.9	77.2 ±1.2
	64	76.1 ±3.1	87.6 ±0.3	84.3 ±0.6	79.7 ±0.3	84.1 ±0.7
	128	85.2 ±2.0	92.4 ±0.7	87.5 ±0.5	87.2 ±0.5	89.1 ±0.4
3	16	79.1 ±1.9	79.0 ±1.9	82.0 ±0.3	80.4 ±0.4	82.1 ±2.1
	32	83.0 ±3.8	87.8 ±0.9	88.6 ±1.2	88.1 ±0.7	87.1 ±0.6
	64	88.4 ±1.5	91.6 ±0.3	90.9 ±0.3	90.8 ±0.6	90.8 ±0.8
	128	91.6 ±1.3	94.0 ±1.2	92.4 ±0.2	93.4 ±1.2	92.8 ±0.8
4	16	81.5 ±2.8	71.5 ±1.0	83.8 ±1.1	83.8 ±0.7	84.7 ±1.2
	32	87.8 ±0.5	83.7 ±1.9	89.4 ±0.4	90.9 ±0.5	90.8 ±1.0
	64	91.9 ±0.8	92.9 ±1.3	93.1 ±0.2	93.4 ±1.0	92.8 ±0.3
	128	94.2 ±0.5	93.3 ±0.3	94.1 ±0.4	94.8 ±0.2	94.4 ±0.1

(a) Accuracy

n_l	n_h	Neural CDE		FlowPath		
		Spline	MLP	ResNet	GRU	Coupling
1	16	39.7 ±3.2	84.6 ±1.1	56.7 ±6.7	52.5 ±4.1	37.1 ±12.5
	32	49.2 ±3.4	87.3 ±0.5	58.5 ±1.8	60.5 ±3.8	60.5 ±1.0
	64	55.4 ±3.9	89.1 ±0.8	69.3 ±1.4	71.8 ±3.2	67.9 ±2.3
	128	67.8 ±3.1	90.0 ±0.9	79.6 ±2.8	79.0 ±1.6	77.1 ±4.9
2	16	54.0 ±7.4	83.4 ±2.3	79.3 ±1.6	77.1 ±1.9	70.2 ±1.9
	32	64.7 ±5.6	87.3 ±0.6	83.3 ±3.0	76.6 ±1.0	78.9 ±0.9
	64	78.8 ±3.1	89.3 ±0.6	86.0 ±0.6	81.8 ±0.7	86.8 ±1.1
	128	87.1 ±1.8	93.6 ±0.6	88.9 ±0.6	88.4 ±0.3	90.5 ±0.5
3	16	82.5 ±1.4	82.1 ±1.8	83.4 ±0.4	82.3 ±0.1	84.8 ±2.2
	32	85.7 ±2.9	89.8 ±0.7	90.1 ±1.1	90.1 ±0.8	89.1 ±0.2
	64	90.3 ±1.2	93.2 ±0.2	92.2 ±0.5	92.5 ±0.6	92.1 ±0.3
	128	93.0 ±0.9	95.2 ±0.9	93.6 ±0.4	94.7 ±0.9	93.8 ±1.1
4	16	84.9 ±2.0	74.5 ±3.0	85.6 ±1.0	86.1 ±0.9	86.6 ±1.3
	32	89.5 ±0.8	85.9 ±1.4	90.9 ±0.2	92.6 ±0.5	92.0 ±1.5
	64	93.3 ±0.6	93.8 ±0.8	94.2 ±0.6	94.4 ±0.9	93.9 ±0.5
	128	95.2 ±0.4	94.2 ±0.2	94.8 ±0.4	95.8 ±0.4	95.1 ±0.3

(b) Precision

n_l	n_h	Neural CDE		FlowPath		
		Spline	MLP	ResNet	GRU	Coupling
1	16	33.7 ±1.7	85.0 ±1.1	55.3 ±4.0	48.4 ±3.7	39.6 ±2.3
	32	44.4 ±2.5	87.6 ±1.0	58.0 ±3.6	60.2 ±5.1	59.9 ±1.7
	64	53.9 ±3.8	88.9 ±0.5	69.0 ±3.9	69.8 ±4.2	67.6 ±1.3
	128	66.0 ±3.0	89.5 ±0.7	79.8 ±2.6	79.0 ±1.7	77.7 ±4.6
2	16	45.5 ±6.1	84.2 ±2.4	80.0 ±2.0	75.7 ±1.4	69.9 ±0.7
	32	62.4 ±7.1	88.3 ±0.2	83.3 ±4.1	76.8 ±1.9	78.6 ±1.5
	64	78.3 ±3.6	89.1 ±0.3	86.2 ±0.9	82.6 ±0.3	85.6 ±1.2
	128	86.9 ±1.7	93.0 ±0.6	88.3 ±0.8	88.3 ±0.9	89.7 ±0.7
3	16	81.3 ±2.1	81.3 ±2.6	84.0 ±0.2	82.0 ±0.2	84.3 ±2.4
	32	84.8 ±3.0	89.1 ±0.8	89.9 ±0.8	89.0 ±0.9	88.0 ±0.8
	64	89.4 ±1.4	92.1 ±0.2	91.9 ±0.3	91.8 ±0.2	91.8 ±0.6
	128	92.3 ±1.3	94.4 ±1.0	93.1 ±0.6	94.3 ±1.1	93.3 ±0.5
4	16	83.5 ±2.6	73.4 ±2.3	85.1 ±0.8	85.2 ±0.6	86.3 ±0.8
	32	89.2 ±0.5	86.0 ±2.0	90.5 ±0.6	91.3 ±0.5	91.7 ±0.9
	64	92.7 ±0.6	93.2 ±1.4	93.6 ±0.4	93.9 ±0.6	93.3 ±0.4
	128	94.8 ±0.5	93.6 ±0.6	94.4 ±0.7	95.5 ±0.2	94.6 ±0.3

(c) Recall

n_l	n_h	Neural CDE		FlowPath		
		Spline	MLP	ResNet	GRU	Coupling
1	16	33.6 ±2.8	84.5 ±1.0	53.5 ±6.1	47.0 ±3.4	34.0 ±6.2
	32	44.8 ±2.4	87.4 ±0.6	57.4 ±2.7	59.9 ±4.4	59.5 ±1.5
	64	54.0 ±3.6	88.9 ±0.5	68.6 ±2.5	70.3 ±3.8	67.6 ±1.7
	128	66.5 ±3.1	89.7 ±0.5	79.5 ±2.7	78.8 ±1.6	77.2 ±4.7
2	16	46.3 ±6.5	83.4 ±2.2	78.9 ±1.2	75.6 ±1.1	69.3 ±0.8
	32	62.5 ±6.9	87.5 ±0.3	83.1 ±3.6	76.5 ±1.3	78.5 ±0.9
	64	78.3 ±3.3	89.1 ±0.2	85.9 ±0.6	82.0 ±0.5	86.1 ±1.0
	128	86.9 ±1.7	93.2 ±0.6	88.5 ±0.8	88.3 ±0.6	89.9 ±0.2
3	16	81.7 ±1.8	81.3 ±2.3	83.5 ±0.2	82.0 ±0.2	84.3 ±2.2
	32	85.0 ±3.0	89.4 ±0.8	90.0 ±0.9	89.5 ±0.8	88.4 ±0.5
	64	89.8 ±1.3	92.6 ±0.2	91.9 ±0.3	92.1 ±0.4	91.9 ±0.3
	128	92.6 ±1.1	94.8 ±0.9	93.3 ±0.5	94.5 ±0.9	93.5 ±0.8
4	16	84.0 ±2.3	71.5 ±3.3	85.2 ±0.8	85.5 ±0.7	86.3 ±1.0
	32	89.2 ±0.5	85.9 ±1.8	90.6 ±0.4	91.8 ±0.2	91.7 ±1.2
	64	93.0 ±0.6	93.5 ±1.1	93.8 ±0.5	94.1 ±0.7	93.5 ±0.4
	128	95.0 ±0.4	93.9 ±0.4	94.6 ±0.5	95.6 ±0.2	94.8 ±0.2

(d) F1 Score

Table 14: Results of hyperparameter tuning for ‘PAMAP2’ with original irregular scenario

Data Preprocessing.

Users one through eight were included in the analysis, while the ninth subject was excluded due to insufficient sensor readings. The signal data were subsequently segmented into units using a 600-second window with a 50% overlap between segments. Initially, the PAMAP2 dataset included 18 daily living activities, but we removed activities represented by fewer than 500 samples, resulting in a dataset with 8 activities. Consequently, the modified PAM dataset comprises 5333 segments of sensor

⁴<https://archive.ics.uci.edu/dataset/231/pamap2+physical+activity+monitoring>

⁵<https://github.com/mims-harvard/Raindrop>

signal data. Each segment is collected from 17 sensors, capturing 600 continuous data points at a 100 Hz sampling rate. To introduce irregularity into the time series, we randomly eliminated 60% of the data points from each segment, ensuring the selection of removed observations was random yet consistent across all experiments.

Comparison with benchmark methods.

Figure 14 and Table 15 present the performance comparison between the proposed method and baseline models under varying sensor missing rates. FlowPath consistently achieves higher classification accuracy and robustness across all levels of missingness. The performance gap widens as the missing rate increases, indicating that learning a structurally-constrained control path is particularly beneficial when observations are sparse.

Methods	0%	10%	20%	30%	40%	50%
Transformer	83.5 ±1.5	60.9 ±12.8	62.3 ±11.5	52.0 ±11.9	43.8 ±14.0	43.2 ±2.5
Trans-mean	83.7 ±2.3	62.4 ±3.5	56.8 ±4.1	65.1 ±1.9	48.7 ±2.7	46.4 ±1.4
GRU-D	83.3 ±1.6	68.4 ±3.7	64.8 ±0.4	58.0 ±2.0	47.7 ±1.4	49.7 ±1.2
SeFT	67.1 ±2.2	40.0 ±1.9	34.2 ±2.8	31.7 ±1.5	26.8 ±2.6	26.4 ±1.4
mTAND	74.6 ±4.3	53.4 ±2.0	45.6 ±1.6	34.7 ±5.5	23.7 ±1.0	20.9 ±3.1
Raindrop	74.3 ±3.8	76.7 ±1.8	71.3 ±2.5	60.3 ±3.5	57.0 ±3.1	47.2 ±4.4
Neural CDE	94.2 ±0.5	85.8 ±1.4	74.4 ±0.5	65.5 ±1.8	55.8 ±0.5	49.9 ±1.7
FlowPath	94.8 ±0.2	86.6 ±1.1	77.0 ±1.7	67.3 ±0.2	58.1 ±0.1	52.0 ±0.6

(a) Accuracy

Methods	0%	10%	20%	30%	40%	50%
Transformer	84.8 ±1.5	58.4 ±18.4	65.9 ±12.7	55.2 ±15.3	44.6 ±23.0	52.0 ±2.5
Trans-mean	84.9 ±2.6	59.6 ±7.2	59.4 ±3.4	63.8 ±1.2	55.8 ±2.6	59.1 ±3.2
GRU-D	84.6 ±1.2	74.2 ±3.0	69.8 ±0.8	63.2 ±1.7	63.4 ±1.6	52.4 ±0.3
SeFT	70.0 ±2.4	40.8 ±3.2	34.9 ±5.2	31.0 ±2.7	24.1 ±3.4	23.0 ±2.9
mTAND	74.3 ±4.0	54.8 ±2.7	49.2 ±2.1	43.4 ±4.0	33.9 ±6.5	35.1 ±6.1
Raindrop	75.6 ±2.1	79.9 ±1.7	75.8 ±2.2	68.1 ±3.1	65.4 ±2.7	59.4 ±3.9
Neural CDE	95.2 ±0.4	88.8 ±1.2	81.0 ±0.8	73.1 ±1.8	67.7 ±1.5	65.5 ±0.8
FlowPath	95.8 ±0.4	89.5 ±0.8	82.4 ±1.4	75.1 ±0.4	67.0 ±0.9	66.3 ±1.9

(b) Precision

Methods	0%	10%	20%	30%	40%	50%
Transformer	86.0 ±1.2	59.1 ±16.2	61.4 ±13.9	50.1 ±13.3	40.5 ±15.9	36.9 ±3.1
Trans-mean	86.4 ±2.1	63.7 ±8.1	53.2 ±3.9	67.9 ±1.8	54.2 ±3.0	43.1 ±2.2
GRU-D	85.2 ±1.6	70.8 ±4.2	65.8 ±0.5	58.2 ±3.1	44.5 ±0.5	42.5 ±1.7
SeFT	68.2 ±1.5	41.0 ±0.7	34.6 ±2.1	32.0 ±1.2	28.0 ±1.2	27.5 ±0.4
mTAND	79.5 ±2.8	57.0 ±1.9	49.0 ±1.6	36.3 ±4.7	26.4 ±1.6	23.0 ±3.2
Raindrop	77.9 ±2.2	77.9 ±2.3	72.5 ±2.0	60.3 ±3.6	56.7 ±3.1	44.8 ±5.3
Neural CDE	94.8 ±0.5	86.3 ±1.3	74.7 ±1.0	64.9 ±2.3	54.5 ±2.3	48.9 ±1.5
FlowPath	95.5 ±0.2	87.4 ±0.4	77.1 ±2.3	67.7 ±0.7	57.1 ±0.7	51.3 ±0.7

(c) Recall

Methods	0%	10%	20%	30%	40%	50%
Transformer	85.0 ±1.3	56.9 ±18.9	61.8 ±15.6	48.4 ±18.2	40.2 ±20.1	41.9 ±3.2
Trans-mean	85.1 ±2.4	62.7 ±6.4	55.3 ±3.5	64.9 ±1.7	55.1 ±2.9	46.5 ±3.1
GRU-D	84.8 ±1.2	72.0 ±3.7	67.2 ±0.0	59.3 ±3.5	47.5 ±0.0	47.5 ±1.2
SeFT	68.5 ±1.8	39.9 ±1.5	33.3 ±2.7	28.0 ±1.6	23.3 ±3.0	23.5 ±1.8
mTAND	76.8 ±3.4	55.9 ±2.2	49.0 ±1.0	39.5 ±4.4	29.3 ±1.9	27.7 ±3.9
Raindrop	76.6 ±2.8	78.6 ±1.8	73.4 ±2.1	61.9 ±3.9	58.9 ±2.5	47.6 ±5.2
Neural CDE	95.0 ±0.4	87.3 ±1.3	76.8 ±0.6	67.1 ±1.9	57.7 ±1.6	51.6 ±1.0
FlowPath	95.6 ±0.2	88.3 ±0.4	79.1 ±1.9	70.0 ±0.7	59.6 ±1.0	54.1 ±1.0

(d) F1 Score

Table 15: Classification performance on PAMAP2 dataset with original and sensor dropout from 10% to 50%

Results of hyperparameter tuning.

Following Zhang et al. (2022), training was performed with a batch size of 128, a learning rate of 0.0001, and 20 epochs. Similar to the previous experiment, we employed grid search for hyperparameter tuning: number of layers $n_l \in \{1, 2, 3, 4\}$, and hidden vector dimensions $n_h \in \{16, 32, 64, 128\}$. The results of this tuning are presented in Table 14, where we discovered that a configuration with $n_l = 4$ layers and $n_h = 128$ hidden vector dimensions yields the optimal performance of F1 Score.

Table 16 presents a performance comparison between the standard Neural CDE, incorporating an MLP-based path, and the proposed FlowPath model in scenarios with missing sensor data. Baseline methods that rely on fixed or unconstrained paths show greater performance degradation, underscoring the advantages of the proposed approach.

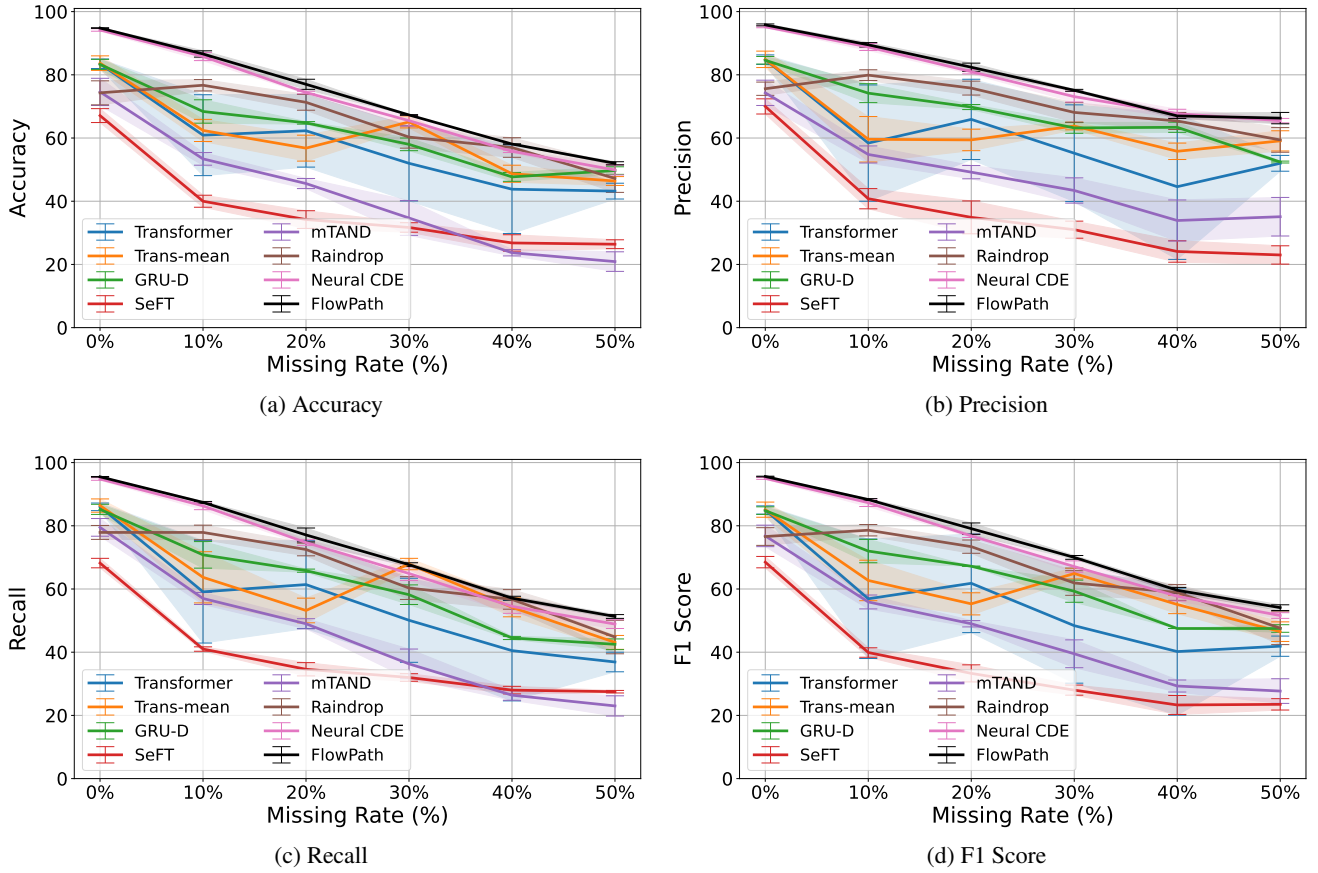


Figure 14: Classification performance of FlowPath compared to baseline models on the PAMAP2 dataset as the percentage of sensor dropout increases. Solid lines indicate the mean performance, and shaded regions represent one standard deviation. FlowPath exhibits superior and more stable performance across all metrics, demonstrating robustness in handling ISTS.

Settings	Neural CDE		FlowPath		
	Spline	MLP	ResNet	GRU	Coupling
Regular	94.2 ± 0.5	93.3 ± 0.3	94.1 ± 0.4	94.8 ± 0.2	94.4 ± 0.1
10% Missing	85.8 ± 1.4	84.8 ± 0.4	86.0 ± 0.3	86.6 ± 1.1	86.0 ± 0.4
20% Missing	74.4 ± 0.5	73.2 ± 0.4	76.7 ± 1.2	77.0 ± 1.7	75.0 ± 0.4
30% Missing	65.5 ± 1.8	65.5 ± 0.2	69.6 ± 0.5	67.3 ± 0.2	67.4 ± 0.3
40% Missing	55.8 ± 0.5	57.5 ± 1.8	63.9 ± 1.7	58.1 ± 0.1	59.0 ± 0.3
50% Missing	49.9 ± 1.7	51.5 ± 2.7	55.1 ± 0.3	52.0 ± 0.6	53.1 ± 2.0

(a) Accuracy

Settings	Neural CDE		FlowPath		
	Spline	MLP	ResNet	GRU	Coupling
Regular	95.2 ± 0.4	94.2 ± 0.2	94.8 ± 0.4	95.8 ± 0.4	95.1 ± 0.3
10% Missing	88.8 ± 1.2	87.6 ± 1.5	88.5 ± 0.5	89.5 ± 0.8	88.1 ± 0.6
20% Missing	81.0 ± 0.8	79.0 ± 1.8	82.3 ± 1.4	82.4 ± 1.4	80.2 ± 1.0
30% Missing	73.1 ± 1.8	74.1 ± 3.8	76.8 ± 1.5	75.1 ± 0.4	74.4 ± 1.7
40% Missing	67.7 ± 1.5	65.9 ± 3.7	70.2 ± 2.1	67.0 ± 0.9	68.0 ± 1.4
50% Missing	65.5 ± 0.8	60.6 ± 2.5	67.4 ± 2.4	66.3 ± 1.9	65.4 ± 2.7

(b) Precision

Settings	Neural CDE		FlowPath		
	Spline	MLP	ResNet	GRU	Coupling
Regular	94.8 ± 0.5	93.6 ± 0.6	94.4 ± 0.7	95.5 ± 0.2	94.6 ± 0.3
10% Missing	86.3 ± 1.3	85.5 ± 0.8	86.4 ± 0.4	87.4 ± 0.4	87.0 ± 0.2
20% Missing	74.7 ± 1.0	73.3 ± 2.1	77.7 ± 1.1	77.1 ± 2.3	76.4 ± 0.5
30% Missing	64.9 ± 2.3	65.7 ± 1.8	68.8 ± 1.4	67.7 ± 0.7	67.9 ± 1.4
40% Missing	54.5 ± 2.3	56.9 ± 2.5	64.2 ± 1.7	57.1 ± 0.7	58.4 ± 1.5
50% Missing	48.9 ± 1.5	48.9 ± 2.4	55.1 ± 0.3	51.3 ± 0.7	51.4 ± 2.7

(c) Recall

Settings	Neural CDE		FlowPath		
	Spline	MLP	ResNet	GRU	Coupling
Regular	95.0 ± 0.4	93.9 ± 0.4	94.6 ± 0.5	95.6 ± 0.2	94.8 ± 0.2
10% Missing	87.3 ± 1.3	86.4 ± 1.0	87.2 ± 0.3	88.3 ± 0.4	87.4 ± 0.3
20% Missing	76.8 ± 0.6	75.1 ± 0.8	79.3 ± 1.0	79.1 ± 1.9	77.8 ± 0.6
30% Missing	67.1 ± 1.9	68.2 ± 0.8	71.4 ± 0.7	70.0 ± 0.7	70.2 ± 1.0
40% Missing	57.7 ± 1.6	58.8 ± 2.8	65.9 ± 1.9	59.6 ± 1.0	60.8 ± 1.1
50% Missing	51.6 ± 1.0	50.7 ± 2.0	57.9 ± 0.2	54.1 ± 1.0	54.2 ± 3.1

(d) F1 Score

Table 16: Performance comparison on ‘PAMAP2’ with different flow configuration